

# Tectonics

## RESEARCH ARTICLE

10.1029/2020TC006355

### Key Points:

- Deformation of the African plate 75 Ma was mainly driven by horizontal gravitational stress, transform shear and weak slab pull
- The weak pull from the Neotethys slab indicates that the slab was short or the pull was reduced by mantle resistance or by slab buoyancy
- The complex closure history of the Neotethys Ocean is a likely candidate for the limited pull magnitude

### Correspondence to:

M. C. Wouters,  
[m.c.wouters@uu.nl](mailto:m.c.wouters@uu.nl)

### Citation:

Wouters, M. C., Pérez-Díaz, L., Tuck-Martin, A., Eagles, G., Adam, J., & Govers, R. (2021). Dynamics of the African plate 75 Ma: From plate kinematic reconstructions to intraplate paleo-stresses. *Tectonics*, 40, e2020TC006355. <https://doi.org/10.1029/2020TC006355>




Received 5 JUN 2020  
 Accepted 30 JUN 2021

### Author Contributions:

**Conceptualization:** Marius C. Wouters, Lucía Pérez-Díaz, Graeme Eagles, Jürgen Adam, Rob Govers  
**Data curation:** Marius C. Wouters  
**Formal analysis:** Marius C. Wouters  
**Funding acquisition:** Rob Govers  
**Investigation:** Marius C. Wouters, Lucía Pérez-Díaz, Graeme Eagles, Rob Govers  
**Methodology:** Marius C. Wouters, Rob Govers  
**Project Administration:** Graeme Eagles, Jürgen Adam, Rob Govers  
**Resources:** Rob Govers  
**Software:** Marius C. Wouters, Rob Govers  
**Supervision:** Lucía Pérez-Díaz, Graeme Eagles, Jürgen Adam, Rob Govers

© Wiley Periodicals LLC. The Authors. This is an open access article under the terms of the [Creative Commons Attribution License](https://creativecommons.org/licenses/by/4.0/), which permits use, distribution and reproduction in any medium, provided the original work is properly cited.

## Dynamics of the African Plate 75 Ma: From Plate Kinematic Reconstructions to Intraplate Paleo-Stresses

Marius C. Wouters<sup>1</sup> , Lucía Pérez-Díaz<sup>2,3</sup>, Amy Tuck-Martin<sup>2</sup>, Graeme Eagles<sup>4</sup> , Jürgen Adam<sup>2</sup>, and Rob Govers<sup>1</sup> 

<sup>1</sup>Tectonophysics Group, Department of Earth Sciences, Utrecht University, Utrecht, The Netherlands, <sup>2</sup>Department of Earth Sciences, Royal Holloway, University of London, Surrey, UK, <sup>3</sup>Department of Earth Sciences, University of Oxford, Oxford, UK, <sup>4</sup>Alfred Wegener Institute, Helmholtz Centre for Polar and Marine Research, Bremerhaven, Germany

**Abstract** Plate reconstruction studies show that the Neotethys Ocean was closing due to the convergence of Africa and Eurasia toward the end of the Cretaceous. The period around 75 Ma reflects the onset of continental collision between the two plates as convergence continued to be taken up mostly by subduction of the Neotethys slab beneath Eurasia. The Owen transform plate boundary in the northeast accommodated the fast northward motion of the Indian plate relative to the African plate. The rest of the plate was surrounded by mid-ocean ridges. Africa was experiencing continent-wide rifting related to northeast-southwest extension. We aim to quantify the forces and paleostresses that may have driven this continental extension. We use the latest plate kinematic reconstructions in a grid search to estimate horizontal gravitational stresses (HGSs), plate boundary forces, and the plate's interaction with the asthenosphere. The contribution of dynamic topography to HGSs is based on recent mantle convection studies. We model intraplate stresses and compare them with the strain observations. The fit to observations favors models where dynamic topography amplitudes are smaller than 300 m. The results also indicate that the net pull transmitted from slab to the surface African plate was low. To put this into context, we notice that available tectonic reconstructions show fragmented subduction zones and various colliding micro-continents along the northern margin of the African plate around this time. We therefore interpret a low net pull as resulting from either a small average slab length or from the micro-continents' resistance to subduction.

## 1. Introduction

The dynamics of tectonic plates is governed by the balance of gravity and friction with surrounding plates and with the asthenosphere. While models for gravitational forcing on plates, that is, slab pull and horizontal gravitational stresses (HGSs), can resolve the magnitudes relatively well (England & Wortel, 1980; Fleitout & Froidevaux, 1982; Frank, 1972; Meijer & Wortel, 1997; Nijholt et al., 2018; Richter & McKenzie, 1978; Wortel et al., 1991), quantification of resistive coupling between plates along different boundary types (Coblentz et al., 1998; Govers & Meijer, 2001; Humphreys & Coblentz, 2007; Van Benthem & Govers, 2010; Warners-Ruckstuhl et al., 2013), and of the tractions on the base of the lithosphere is not trivial (Conrad & Lithgow-Bertelloni, 2006; Flament et al., 2013; Forsyth & Uyeda, 1975; Molnar et al., 2015; Moucha & Forte, 2011; Phillips & Bunge, 2005; Van Summeren et al., 2012). Even though the most apparent surface deformation generally occurs along convergent plate boundaries, tractions on plate boundaries have been shown to influence the stresses throughout the lithosphere (Coblentz & Richardson, 1995; Zback, 1992), causing remote intraplate deformation, especially in cases where strong lithosphere is transmitting stress (England & Houseman, 1985; Neil & Houseman, 1997). Thus, plate boundary forces are crucial in the analysis of deformation in the plate interiors.

Various studies of the evolution of the African plate have tried to link plate kinematic reconstructions directly to observations of tectonic activity (e.g., Guiraud & Bosworth, 1997; Guiraud et al., 2005; Janssen et al., 1995). However, deducing the tractions and corresponding stresses directly from plate kinematics is impossible without a proper description of the coupling on plate contacts, which is a highly nonlinear function of plate boundary rheologies. Thus, meaningfully linking kinematics directly to geological observations is impossible too. Fortunately, we can constrain traction magnitudes by applying the basic assumption

**Validation:** Marius C. Wouters, Rob Govers

**Visualization:** Marius C. Wouters

**Writing – original draft:** Marius C. Wouters, Rob Govers

**Writing – review & editing:** Marius C. Wouters, Lucía Pérez-Díaz, Amy Tuck-Martin, Graeme Eagles, Jürgen Adam, Rob Govers

that tectonic plates are in mechanical equilibrium (Chapple & Tullis, 1977; Forsyth & Uyeda, 1975). This torque balance criterion has been previously applied by numerous authors to relate tectonic forces to the kinematics and deformation, both for present and past situations of various tectonic plates including the Pacific (Stotz et al., 2017, 2018; Wortel et al., 1991), Juan de Fuca (Govers & Meijer, 2001), South America (Coblentz & Richardson, 1996; Meijer & Wortel, 1992; Stefanick & Jurdy, 1992), Caribbean (Van Benthem & Govers, 2010), Farallon (Wortel & Cloetingh, 1981), North America (Richardson & Reding, 1991), Eurasia (Warners-Ruckstuhl et al., 2013), Africa (Meijer & Wortel, 1999; Stamps et al., 2015), India (Copley et al., 2010), and Australia (Coblentz et al., 1995). The analysis of the African plate by Meijer and Wortel (1999) focused on the correlation between the observational record of the Africa-Eurasia collision history and the forces on the rest of the plate, but did not resolve tractions at the northern convergent boundary. Gaina et al. (2013) studied the evolution of African plate boundary lengths, the plate's absolute velocity, and the distribution of oceanic crustal ages since the Jurassic. They also presented paleo-stress models for the plate 68 Ma, but did not constrain their models by torque balance, which both impairs the reliability of their stresses and the ability to relate their results to tractions on the plate boundaries.

Here, our goal is to determine the distribution of tractions along plate boundaries of the African plate in the Late Cretaceous and their influence on intraplate stresses and deformation. The nature of the northern plate boundary is a specific point of attention in our analysis.

Toward the end of the Cretaceous, the African plate was bounded by the convergent Neotethyan boundary in the north, the Owen oceanic transform fault in the northeast and mid-ocean ridges along the rest of the boundaries, as shown in Figure 1 (Seton et al., 2012). The selected 75 Ma, Campanian age, saw the onset of collision following closure of oceanic basins between Africa and Eurasia, which had a large influence on the later Cenozoic evolution of the region (Stampfli et al., 2002; Van Hinsbergen et al., 2019). The work presented here is part of a project aiming to constrain the evolution of collision forces in the western Tethyan region. Additionally, the choice for the 75 Ma age is based on the degree of confidence in nature and geometry of Africa's boundaries at the time. Seafloor spreading in the Mascarene basin between India and Africa was well established, while for older ages (>89 Ma) India was still attached to Africa (Tuck-Martin et al., 2018).

The torque balance criterion cannot constrain the tractions fully to a single unique solution. Therefore, we perform a grid search over the torque balance solution space, to explore the range of possible tractions. In addition, we explore the influence of dynamic topography on the balance and the intraplate stresses. Intraplate stresses are computed for all balanced models in the grid search. To validate the models, we compare the stresses with geological observations. While studies modeling present-day lithosphere dynamics can validate their results against present-day stress observations, as conveniently compiled in the World Stress Map (Heidbach et al., 2016), we are limited to observations of strain orientations associated with historical geological events. Intraplate deformation during the selected time frame was mostly confined to NW-SE trending rifts throughout Africa (Guiraud & Bosworth, 1997; Janssen et al., 1995). In combination with the physical constraints, we constrain the main forces that moved and deformed Africa at the end of the Cretaceous.

## 2. Tectonic Setting

During the Campanian, seafloor spreading around Africa was well established (Figure 1). Seafloor spreading between Africa and South America, which started around 138 Ma between the southernmost parts of the continents, had progressed northward reaching the central Atlantic gateway by 100 Ma (Pérez-Díaz & Eagles, 2014). In the Indian Ocean, divergence between Madagascar and India along the Mascarene ridge became established soon after, around 89 Ma (Tuck-Martin et al., 2018). The tectonic situation of the northern convergent boundary of the African plate was complex (e.g., Stampfli et al., 2002; Van Hinsbergen et al., 2019). While it seems clear that closure of the Neotethys Ocean was being accommodated by some combination of subduction and incipient Alpine collision between the Adria micro-continent(s) and the European plate, the presence of Neotethyan micro-continent(s) means there is no consensus on the geometry and evolution of the plate boundary with Eurasia. The uncertainties in this area stem from the fact that much of the Neotethyan lithosphere has been subducted, and thus information on the past composition has been lost. Seton et al. (2012) provides a first-order reconstruction of the collision, as shown in the northern

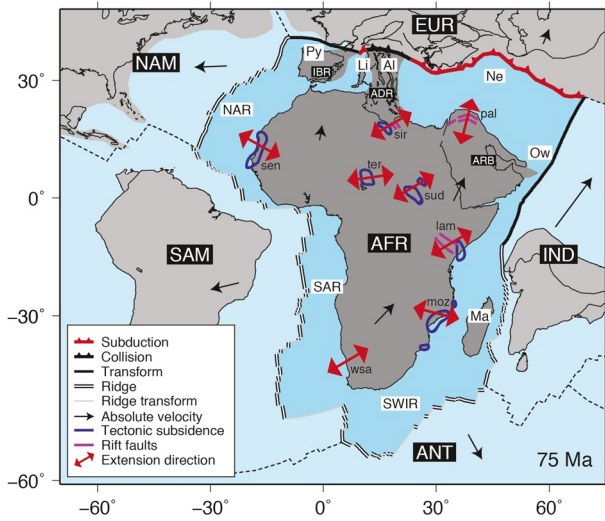


**Figure 1.** Tectonic setting of the African plate 75 Ma. Locations of geological observations of tectonic subsidence (Janssen et al., 1995), other rift basins with active faults (Abadi et al., 2008; Bosworth & Morley, 1994; Brew et al., 2003), and regional extension (Viola et al., 2012) and their corresponding extension directions are also shown. Plate abbreviations: ADR, Adria; AFR, Africa; ANT, Antarctica; ARB, Arabia; EUR, Europe; IBR, Iberia; IND, India; NAM, North America; SAM, South America. Abbreviations of the plate boundaries: Al, Alpine collision boundary; Li, Ligurian subduction zone; Ma, Mascarene ridge; NAR, northern mid-Atlantic ridge; Ne, Neotethys subduction zone; Ow, Owen transform fault; Py, Pyrenees transform fault; SAR, southern mid-Atlantic ridge; SWIR, ancestral southwest Indian ridge. Abbreviations of rifting locations: lam, Lamu embayment and Anza rift (Kenya); moz, Mozambique basins; pal, Palmyride and Euphrates basins (Syria); wsa, western South African margin; sen, Senegal basin; sir, Sirt basins (Libya); sud, Sudan rifts (South Sudan); ter, Termit trough (eastern Niger). The reconstruction is a compilation of the kinematic reconstructions of SAM-AFR by Pérez-Díaz and Eagles (2014), ANT-AFR and IND-AFR by Tuck-Martin et al. (2018) and EUR-AFR and NAM-AFR by Seton et al. (2012).

part of Figure 1. This reconstruction features a large Neotethyan subduction zone, separated from a smaller subduction zone in the Ligurian Ocean, east of Iberia, by a single strip of micro-continent (Adria), which is colliding with Eurasia. For simplicity, we set up our model using the reconstruction of Seton et al. (2012), and choose to interpret the range of slab pull forces that it permits in terms of alternative collisional geometries like those presented by Stampfli et al. (2002) and Van Hinsbergen et al. (2019) (see Section 3.3).

According to the reconstruction of Seton et al. (2012), relative motion between Eurasia and Iberia, while minor, was occurring along the Pyrenees transform fault (see Figure 2). Arabia was still attached to Africa and would only start separating around 30 Ma as a part of the East African Rift system (Bosworth & Stockli, 2016). The spreading ridge in the Mascarene basin was connected to the Neotethys subduction zone by a long sinistral oceanic transform fault, the Owen transform.

Around 84 Ma (Santonian), Africa experienced an intraplate compressional event recognized in an overall transition from subsiding basins to folding and the formation of unconformities (Bosworth et al., 1999; Guiraud & Bosworth, 1997). The event has commonly been linked to a shift in relative movement between Africa and Europe related to a global plate reorganization, and to the onset of Alpine collision (Bosworth et al., 1999; Guiraud & Bosworth, 1997; Guiraud et al., 2005; Janssen et al., 1995).

Faults in rift basins throughout continental Africa were reactivated during the Campanian and Maastrichtian (80–70 Ma). The dominant strike of the affected rifts is NW-SE, indicating a general NE-SW oriented tensional intra-plate stress regime. According to Guiraud and Bosworth (1997) the plate-wide synchronicity of the onset of rifting and the lack of associated volcanism indicates that rifting was not related to mantle plumes, but instead caused by far-field stresses due to plate boundary forces. Janssen et al. (1995) differentiated between rifted basins experiencing thermal and tectonic subsidence, from backstripping analysis. Figure 1 shows a compilation of these tectonically active basins and other active basins not surveyed by Janssen et al. (1995): the Anza rift (Bosworth &

Morley, 1994), Palmyride and Euphrates basins (Brew et al., 2003) and an additional part of the Sirt basin (Abadi et al., 2008). Fault slip measurements indicate that NE-SW oriented extension was also affecting western South Africa, although large-scale rifting did not develop (Viola et al., 2012).

While describing the rifts, the above authors related them directly to a tensional deviatoric stress regime with a most tensional horizontal stress ( $S_{Hmin}$ ) perpendicular to the strike of the rifts. However, stresses are known to preferentially reactivate existing faults (rejuvenation), even in an oblique sense, rather than to form new faults. Evidence for such oblique rifting, for example, from sets of smaller normal faults in the interior of a rift oriented at an angle to its margins (Brune, 2014; Tron & Brun, 1991; Withjack & Jamison, 1986), is more difficult to recognize than that for the main normal rift faults, and could, therefore, have been overlooked. This imposes an inherent uncertainty on deducing past stress orientations from observations of strain. As a consequence, we attribute a significant directional uncertainty to the observations when comparing them to our modeled stresses (Appendix B).

### 3. Methods

Our analysis of Africa's dynamics consists of two parts. In the first part, we identify physically realistic sets of tectonic forces that yield torque balance of the African plate. In the second part, the balanced force sets are used to calculate the resulting stresses, which are compared with the strain observations. We focus on

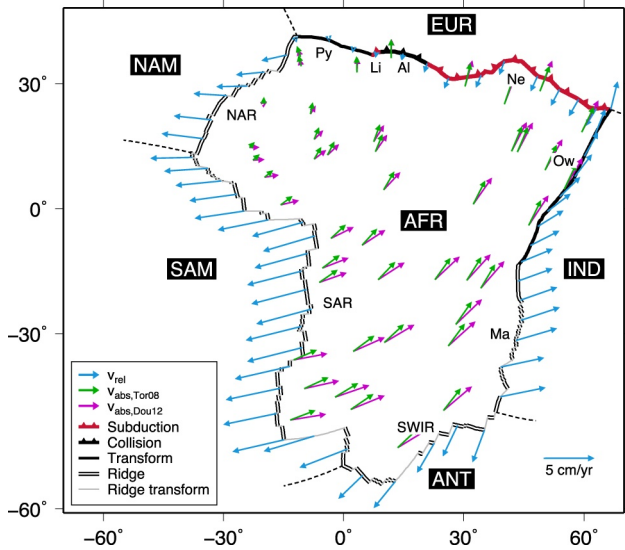


**Figure 2.** Geometry of African plate boundaries and velocities 75 Ma. Both relative velocities ( $v_{rel}$ ) of the surrounding plates with respect to Africa from our reconstruction (compiled from Pérez-Díaz & Eagles, 2014, Tuck-Martin et al., 2018, and Seton et al., 2012) and the absolute velocities of Africa with respect to the asthenosphere by Torsvik et al. (2008) and Doubrovine et al. (2012),  $v_{abs,Tor08}$  and  $v_{abs,Dou12}$ , are plotted. Plate boundary abbreviations as in Figure 1. AFR, Africa; ANT, Antarctica; EUR, Europe; IND, India; NAM, North America; NAR, northern mid-Atlantic ridge; SAM, South America; SAR, southern mid-Atlantic ridge; SWIR, ancestral southwest Indian ridge.

lithospheric averages of horizontal stress, and, likewise, limit our analysis to horizontal components of the forces.

### 3.1. Torque Balance

The modeled African plate 75 Ma is subject to shear tractions at its edges (due to the interaction with neighboring plates), pull from one or multiple subducting slabs, and shear tractions between the base of the plate and the underlying asthenosphere. We specify line forces along plate boundaries. Line forces are the down-dip integrals of the tractions that act on the plate boundary interfaces, that is, forces per unit strike length. As our study concerns the deformation and stresses in the surface part of the plate, slabs are not included in the model (Figure 2). The mechanical effect of the slabs on the surface part of the African plate is represented by line forces along the trench.

Lateral variations in the density of the lithosphere cause changes in gravitational potential energy (GPE). Horizontal GPE gradients contribute to significant spatial variability in horizontal stress (Artyushkov, 1973; Fleitout & Froidevaux, 1982; Frank, 1972), which we refer to as HGS. Physically, the HGSs represent the horizontal gradients of the depth integrated tractions on vertical interfaces and have the physical units Pascal. The ridge push force is a HGS that was derived specifically for oceanic lithosphere (Artyushkov, 1973; Jacoby, 1970; Lliboutry, 1969; Richter & McKenzie, 1978). The HGSs due to crustal thickness variations (Artyushkov, 1973; England & McKenzie, 1982; Molnar & Lyon-Caen, 1988) are sometimes referred to as “gravity collapse forces,” of which HGSs by passive margins are an even more specific case (Sandiford & Colblentz, 1994). We do not distinguish these specific cases and compute the HGSs in all parts of the African plate from horizontal gradients in GPE (see Section 3.7).

To obtain mechanical equilibrium, the torques on a plate with respect to the center of the Earth must sum to zero (Chapple & Tullis, 1977; Forsyth & Uyeda, 1975). For the line forces ( $\vec{F}_{L,i}$ ), basal mantle tractions ( $\vec{\tau}_{dr}$ ) and HGSs ( $\vec{\sigma}_{HGS}$ ), with their corresponding torques  $\vec{T}_{L,i}$ ,  $\vec{T}_{dr}$  and  $\vec{T}_{HGS}$ , the mechanical equilibrium is:

$$\sum_{i=1}^{N_L} \vec{T}_{L,i} + \vec{T}_{dr} + \vec{T}_{HGS} = \sum_{i=1}^{N_L} \int_B \vec{r} \times \vec{F}_{L,i} dB + \int_A \vec{r} \times \vec{\tau}_{dr} dA + \int_A \vec{r} \times \vec{\sigma}_{HGS} dA = \vec{0} \quad (1)$$

where  $N_L$  is the number of line force types,  $\vec{r}$  denotes the position vectors of the forces from the center of the Earth to where they act at the surface,  $B$  is the plate boundary section, and  $A$  the plate area. We distinguish different line force types (the different edge forces and slab pull) based on tectonic setting. Although not all force magnitudes are well constrained, their directions ( $\hat{f}$  or  $\hat{\tau}$ ) can be estimated from either the relative motion between Africa and the adjacent plates, Africa’s absolute motion, or the orientation of the boundary segment, depending on the mechanism (for detail on the directions, see Sections 3.3–3.6). Assuming constant forces along segments, the torque balance Equation 1 becomes:

$$\sum_{i=1}^{N_L} F_{L,i} \int_B \vec{r} \times \hat{f}_{L,i}(\vec{r}) dB + \tau_{dr} \int_A \vec{r} \times \hat{\tau}_{dr}(\vec{r}) dA + \int_A \vec{r} \times \vec{\sigma}_{HGS}(\vec{r}) dA = \sum_{i=1}^{N_L} F_{L,i} \vec{T}'_{L,i} + \tau_{dr} \vec{T}'_{dr} + \vec{T}_{HGS} = \vec{0} \quad (2)$$

where the first integral is taken over the unit edge force vectors and the second integral over the unit basal traction directions, leading to the so-called geometrical torques ( $\vec{T}'$ ; which themselves are not unit vectors). The average line force magnitudes ( $F_{L,i}$ ) and the average basal traction magnitude ( $\tau_{dr}$ ) are the scaling factors of the geometrical torques. Since the geometrical torques are based on our modeled  $\hat{f}_{L,i}$  and  $\hat{\tau}_{dr}$  directions, imposing negative scaling factors would effectively invert those directions, for example, generating forces

aiding the relative motion they should be resisting. Because of this, only positive scaling factors are considered physically realistic. With this formula of torque balance, the better-known scaling factors are used to solve for the poorly constrained scaling factors.

The line forces associated with shear along the plate boundary faults (edge forces) are among the force types we aim to constrain in our models. Tectonic plate boundaries juxtapose complete lithospheres. Plate boundary deformation processes consequently involve both brittle and viscous shear traction contributions (e.g., Behn et al., 2007). Kinematic friction results in shear tractions that are largely independent of slip rate in brittle parts of the plate boundary zone on geological time scales (Niemeijer et al., 2016). In viscous parts of the fault zone, shear tractions from kinematic friction obey a power-law relationship to the relative plate velocity (Kohlstedt et al., 1995). Here we assume that the edge forces are velocity independent, that is, that the brittle shear tractions are dominant.

### 3.2. Plate Reconstructions and Kinematics

In our reconstruction of Africa 75 Ma, locations, geometries, and types of plate boundaries between Africa and its neighboring plates are adopted from recent high resolution kinematic reconstructions of SAM-AFR by Pérez-Díaz and Eagles (2014), ANT-AFR and AFR-IND by Tuck-Martin et al. (2018), and EUR-AFR and NAM-AFR by Seton et al. (2012). For the most part determining the plate boundary type is trivial, as Africa was almost completely surrounded by oceanic ridges 75 Ma. However, the tectonic situation along the Neotethyan boundary is more uncertain, with the possibility of a complex interplay of subduction zones and microcontinents between Africa and Eurasia. We follow the relatively simple reconstruction by Seton et al. (2012) for the plate boundary types at the Neotethyan boundary. According to Seton et al. (2012), Vissers and Meijer (2012), and Macchiarelli et al. (2017), the period around 75 Ma saw little relative motion between Iberia and Africa. Van Hinsbergen et al. (2019) also find that the motion between Africa and Europe in the western Mediterranean was almost entirely accommodated in the Pyrenees. As the possible relative motion does not affect the validity of the torque balance (it holds for multiple plates too), we take Iberia to be attached to Africa. In the coming sections, we discuss the tectonic forces associated with the various plate boundary types. The reconstructions by Tuck-Martin et al. (2018), Pérez-Díaz and Eagles (2014), and Seton et al. (2012) also provide oceanic age, which is crucial for computing HGSs and slab pull.

To constrain the line force and traction directions ( $\hat{f}$ ,  $\hat{\tau}$ ), both Africa's absolute velocity and its velocities relative to neighboring plates are required (Figure 2). The relative velocities in our reconstruction are derived from Pérez-Díaz and Eagles (2014), Tuck-Martin et al. (2018) and Seton et al. (2012). Because Africa's absolute motion rotation pole is close to the plate, the absolute motion vectors are particularly sensitive to the exact location of the rotation pole. To investigate this sensitivity, we consider the absolute motions defined by two recent global moving hotspot frames, by Torsvik et al. (2008) and Doubrovine et al. (2012). Both the relative and absolute velocities are displayed in Figure 2.

Some plate reconstructions feature a double subduction zone between India and Eurasia during the studied period (Jagoutz et al., 2015), as interpreted from ophiolites in the Himalayas (e.g., Beck et al., 1996; Corfield et al., 2001) and seismic tomography (Van Der Voo et al., 1999). Stampfli and Borel (2004) also suggested the presence of a mid-ocean ridge between the two subduction zones in their reconstruction. A second subduction zone would effectively decouple the continental part of the Indian plate from a separate oceanic (Spon-tang/Kshiroda) plate in the northern Neotethys. Thus, relative velocities between India and Africa along the Owen transform are uncertain and could have been lower than reconstructed in Seton et al. (2012). However, since the modeled transform resistance is independent of velocity magnitudes in this study, the implications of the relative velocity uncertainty along the Owen transform are limited.

### 3.3. Subduction and Collision Scenarios for the Neotethys Plate Boundary

In the reconstruction by Seton et al. (2012), subduction occurred at the Eurasian margins of the Neotethys and Ligurian Oceans (Figure 1). The associated slab pull is modeled as line forces acting perpendicular to the trench, quantified by integration of the slab densities, from the trench to the end of the slab. Thus, the magnitude of slab pull will be strongly dependent on the length of slab attached to the African plate. However, alternative reconstructions (e.g., Stampfli et al., 2002; Van Hinsbergen et al., 2019) display more

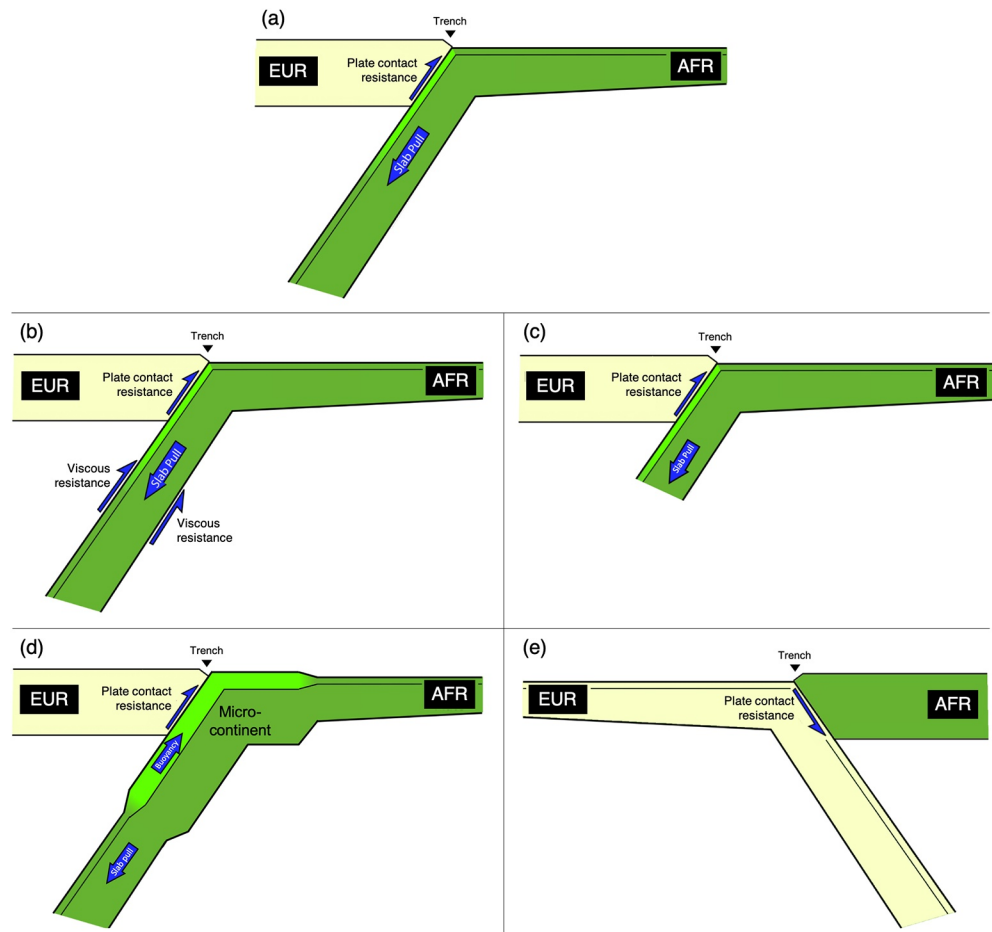


**Figure 3.** Schematic illustrations of the situation leading to maximum slab pull ( $\vec{F}_{L,sp}$ ) (a) and the mechanisms that might lower net slab pull on the African plate ( $\vec{F}_{L,msp}$ ) (b–e): viscous resistance by the mantle (b), slab break-off leading to slab shortening (c), subduction of a micro-continent (d), and subduction polarity reversal (e). AFR, Africa; EUR, Europe.

complex Neothetys subduction settings, involving small closing basins associated with shorter slabs, that could have led to scenarios of reduced slab pull experienced by the plate (Figures 3b–3e). To approach this problem, we initially model the slab pull based on the reconstruction by Seton et al. (2012), as we expect their simple geometry of a large continuous subduction zone to represent the situation with the maximum possible slab pull ( $\vec{F}_{L,sp}$ ; Figure 3a). Then, in Section 3.3.2, we incorporate the reduction in slab pull we might expect to associate with the more complex reconstructions, by scaling back the pull to arrive at a “net slab pull” ( $\vec{F}_{L,msp}$ ).

### 3.3.1. Finding the Maximum Slab Pull

In modeling the maximum possible slab pull ( $\vec{F}_{L,sp}$ ), a density profile at the trench is constructed from a GDH1 geotherm (Stein & Stein, 1992) associated with the lithospheric age at the trench (Figure 4a). Conductive heating of the slab in the mantle, lowering the density contrast between the slab and surrounding mantle with depth, is also integrated, as described by Wortel et al. (1991) and Govers and Meijer (2001). As slabs start to buckle and stagnate above the lower mantle (Fukao & Obayashi, 2013; Fukao et al., 2009), due to phase transformations in the transition zone or increased lower mantle viscosity (King et al., 2015), we assume that lower mantle slabs are completely supported, and, thus, do not contribute to slab pull, in the same way as Conrad and Lithgow-Bertelloni (2002), Conrad et al. (2004), Goes et al. (2011), and Van Summeren et al. (2012). There are no data on the dip angle of the slabs 75 Ma, but Lallemand et al. (2005) found that the average dip of the present-day upper mantle slabs with continental overriding plates is  $50 \pm 20^\circ$ .

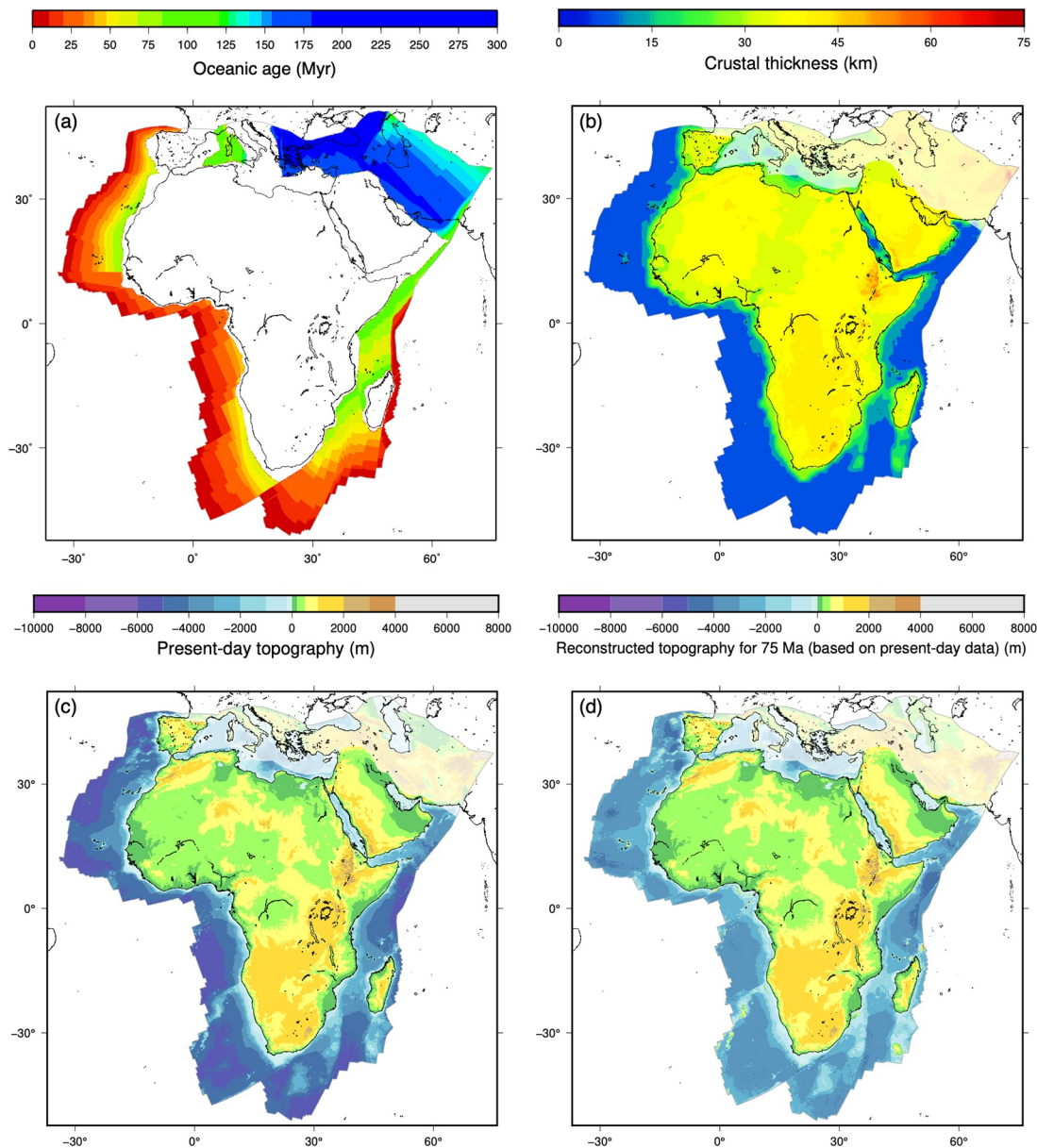


**Figure 4.** Data sets for the calculation of the slab pull forces (a) and horizontal gravitational stresses (a–d). All are plotted with Africa fixed in its present-day position. (a) Ages of the oceanic lithosphere at 75 Ma. The age distribution is a compilation of age grids by Pérez-Díaz and Eagles (2017), Seton et al. (2012), and the age distribution derived from the kinematic model of Tuck-Martin et al. (2018). (b) Present-day crustal thickness map derived from Globig et al. (2016) for the African and Arabian continents and from CRUST1.0 (Laske et al., 2013) for the rest of the continents and the oceanic parts. (c) Present-day topography and bathymetry of GEBCO\_2014 (Weatherall et al., 2015). (d) Reconstructed topography and bathymetry by removing oceanic subsidence since 75 Ma from the present-day bathymetry. We did not attempt to correct the continental topography for Cenozoic tectonics, for example, in East Africa. The light-shaded areas on the crustal thickness and topography maps indicate the uncertain Neotethys area where the present-day data strongly differ from the 75 Ma situation.

They found no correlation between slab dip and oceanic age at the trench, but they did identify that slabs tend to dip shallower, up to roughly  $15^\circ$ , when the overriding plate's absolute velocity is toward the subducting plate. Even though reconstructed absolute motion of Eurasia 75 Ma differs between studies (Williams et al., 2015), the velocity magnitude tends to be low. Because of this uncertainty, we take a conservative approach in calculating the maximum slab pull by choosing a relatively shallow slab dip of  $45^\circ$ . At shallow depths, where the slab is in contact with the overriding plate, the dip angle tends to be lower. Following Lallemand et al. (2005), we choose a dip of  $25^\circ$  for the shallow, megathrust portion of the slab.

The maximum upper mantle slab length is estimated from the consumed oceanic lithosphere in the plate reconstructions of Seton et al. (2012). Their reconstruction shows continuous subduction of the Neotethys Ocean between Africa (Libya and Egypt) and Eurasia from its initiation 160–140 Ma until 75 Ma, associated with approximately 1,300 km of convergence. Between Arabia and Eurasia, more than 2,000 km of convergence occurred after 130 Ma.

Since the length of subducted Neotethyan oceanic lithosphere is large enough (>1,000 km) for the slab to have reached the transition zone, slab pull is modeled to a depth of 670 km. The amount of convergence reconstructed by Seton et al. (2012) in the Ligurian Ocean is much smaller: roughly 250 km of oceanic lithosphere was consumed in the subduction zone between 160 and 75 Ma. Given the small dip angle in the shallow parts of slabs, our modeled Ligurian slab only penetrates up to a depth of 100 km, remaining in contact with the overriding lithosphere and thus contributing less to the slab pull.

### 3.3.2. Scenarios Causing a Reduction in Net Slab Pull

Viscous shear resistance ( $\vec{F}_{L, vr}$ ) acts on the surface enveloping the slab (Figure 3b). In addition, there is resistance from phase changes in the mantle and from corner flow induced by the subduction. We model the overall contribution of the resistance as horizontal line forces at the trench with directions opposite to the absolute motion of Africa. Another possible cause for a low net slab pull is that the slab was shorter (Figure 3c) than reconstructed from Seton et al. (2012). In light of the potential involvement of microcontinents in the closure of the Neotethys, this seems particularly plausible as the entry of young oceanic or continental lithosphere into subduction zones can lead to slab tearing and break-off (e.g., Pallares et al., 2007; Wortel & Spakman, 2000). Detached slab remnants could, however, induce suction forces on the plate at the surface via the mantle flow induced by the sinking remnant (Conrad & Lithgow-Bertelloni, 2002). The suction associated with slab break-off effectively causes the net slab pull to reduce less than it would if there was a break-off without slab suction. Alternatively, subduction of microcontinents could occur instead of slab break-off (Capitanio et al., 2010; Van Hinsbergen et al., 2005). In instances like this, the buoyancy of the subducting microcontinental lithosphere would counteract the slab pull, hence decreasing the net slab pull force (Figure 3d). Some reconstructions of the Eurasian collision zone suggest a reversal in the polarity of subduction (Figure 3e, e.g., Stampfli et al., 2002; Van Hinsbergen et al., 2019). A reversal like this would leave no slab attached to Africa, so naturally there would be no net slab pull. Viscous dissipation of bending stresses (Buffett, 2006; Buffett & Becker, 2012; Conrad & Hager, 1999), could also contribute to a reduction in slab pull. So, it is also implicitly incorporated in the net slab pull formula.

Preliminary experiments showed that the torque directions of slab pull ( $\vec{T}_{L, sp}$ ) and viscous resistance ( $\vec{T}_{L, vr}$ ) were almost antipodal. Therefore, we incorporate viscous resistance into the overall net slab pull torque ( $\vec{T}_{L, nsp}$ ). This  $\vec{T}_{L, nsp}$  is modeled in the direction of the maximum slab pull, with its magnitude scaled back from the magnitude of maximum slab pull ( $T_{L, sp}$ ). The net slab pull torque magnitude ( $T_{L, nsp}$ ) is constrained by the torque balance. The other scenarios of Figure 3 also reduce the net slab pull, and are thus indistinguishable from the contribution of viscous resistance in the net slab pull magnitude results. Scaling the torque magnitude probably does not capture the full effect of the slab pull reducing scenarios, which could also influence the torque direction in cases where the slab pull reduction is not homogeneous along the boundary. However, as the slab pull reduction and torque direction uncertainty increase, the net slab pull torque magnitude will decrease, limiting the effect the torque direction uncertainty has on the overall torque balance result.

Shear along the megathrust is modeled separately from the net slab pull. The direction of this plate contact resistance ( $\vec{F}_{L, per}$ ) line force is modeled opposite to the relative motion at the boundary.

### 3.4. Transform Faults

Shear tractions resist relative plate motion at transform plate boundaries. We model transform shear ( $\vec{F}_{L, tr}$ ) as line forces oriented in the opposite direction to the component of relative motion along the fault. We assume that relative velocity components perpendicular to transform faults do not generate additional fault-perpendicular tractions. This assumption is supported by a study of the Juan de Fuca plate where there



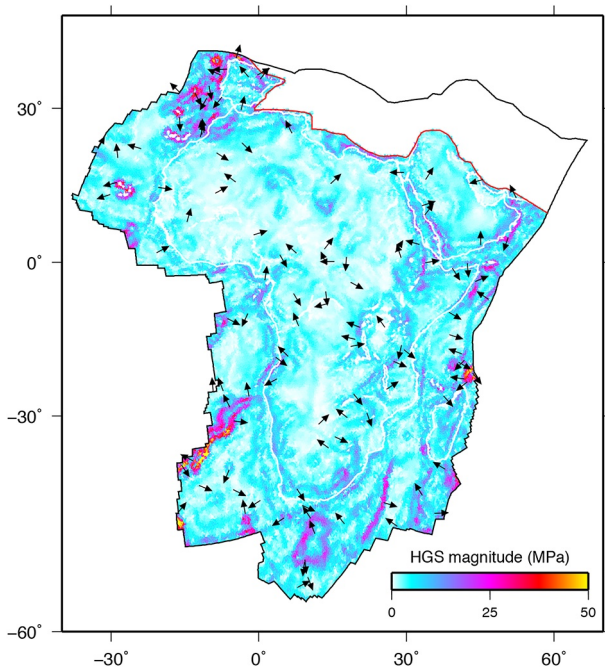


**Figure 5.** Distribution of the horizontal gravitational stresses (HGSs) in the 75 Ma paleogeographical coordinates. A selection of traction directions is represented by black arrows. We exclude the Neotethyan tractions due to the large uncertainty in the HGS results there. Present-day coastlines rotated to the 75 Ma frame are shown in white. A low-pass filter with a lower bound at 100 km is applied to the HGS field.

found that, for the present-day African plate, asthenospheric flow that is solely induced by shear from plate motions leads to a better fit to observed plate velocities than flow imposed by mantle convection models. The shear tractions induced by the former type of asthenospheric flow are almost identical in pattern to the traction pattern induced by our simple passive drag formula. Therefore, and because reconstructed asthenospheric flow for 75 Ma is even more uncertain than that at the present-day, we only apply passive drag in the torque balance. If the results show the requirement for active drag in the torque balance, we can reconsider our decision to disregard it (see Section 5.4).

### 3.7. Horizontal Gravitational Stresses

The calculation of the GPE field and resulting HGSs ( $\bar{\sigma}_{\text{HGS}}$ ; Figure 5) is based on the assumption of lithospheric isostasy, as by Nijholt et al. (2018) and Warners-Ruckstuhl et al. (2012), modified by dynamic topography. The present-day African lithospheric thickness has substantial lateral variability (Globig et al., 2016), and it is likely that lateral variability existed in 75 Ma too. While we use the oceanic ages (Figure 4a) with the oceanic cooling model GDH1 (Stein & Stein, 1992) to compute lithospheric mantle thicknesses in the oceanic parts of the plate, the continental lithospheric thickness variations are not accounted for in our calculation of GPE contrasts, and we consequently underestimate continental HGSs. We estimate that this underestimate is not larger than a factor of two. Because of this, and in the context of the uncertain continental structure for Africa 75 Ma, the resulting HGS fields are thus a first-order approximation. We refer to the supporting information of Nijholt et al. (2018) and Appendix A for details on the HGS computation.

Since data on the crustal thickness distribution are unavailable for 75 Ma Africa, we are restricted to present-day observations (Figure 4b). Crustal thicknesses of the African and Arabian continents are from Globig et al. (2016), who used elevation and geoid data and seismic observations. For the remaining continental

is no evidence for “transform push” along the Mendocino transform fault despite a significant cross-axial convergent component in the motion of the Pacific plate (Govers & Meijer, 2001).

Besides the Owen and Pyrenees transforms, transform faults also link up sections of the mid-ocean ridges (Figure 1). The resistance by these ridge transforms ( $\bar{F}_{L,\text{rif}}$ ) is modeled in the same way as  $\bar{F}_{L,\text{tf}}$ , but we solve the magnitude separately, because the ridge transforms separate younger (Figure 4a), and thus thinner, oceanic lithosphere than the major transforms.

### 3.5. Continental Collision

Collision zones have a distinct fault perpendicular component of motion. In the case of the Alpine collision, the shear component (Figure 2) is indeed very small (<0.2 cm/yr). Hence, we only model the compressional line forces ( $\bar{F}_{L,\text{cc}}$ ), against the normal components of the relative motion directions.

### 3.6. Basal Drag

Basal drag ( $\bar{\tau}_{\text{dr}}$ ) is the traction that arises from the horizontal component of asthenospheric traction on the base of the lithosphere. A hypothetical stationary asthenosphere would induce a passive mantle drag with a direction opposite to the absolute plate velocity. However, the mantle is not stationary and, for some plates, interaction between convective mantle flow and the lithosphere (active drag) has actually been shown to be a requirement for torque balance (e.g., the Eurasian [Warners-Ruckstuhl et al., 2010] and Pacific [Stotz et al., 2018] plates). Stamps et al. (2015)

and oceanic crust, thicknesses are from the CRUST1.0 model (Laske et al., 2013), based on seismic and gravity data, with statistical averages of crustal thickness for unsampled regions.

Topography and bathymetry are also required, and again, we are mostly limited to present-day observations (Figure 4c), using the digital elevation model of GEBCO\_2014 (Weatherall et al., 2015). In addition, the amount of oceanic subsidence during the 75 Myr between the studied age and the data is approximated with the oceanic cooling model GDH1 (Stein & Stein, 1992) and the oceanic ages of Figure 4a. The reconstructed bathymetry, with the subsidence removed, is displayed in Figure 4d. In Section 5.3, we investigate the influence of different length scales of HGS uncertainties (like those generated by using present-day topography and crustal thickness) on the modeled HGS torque and stresses.

The uncertainty regarding the exact shape and type of the African plate's northern boundary in the Neotethys makes constraining crustal thickness and topography of the area practically impossible, as indicated by the light shaded areas in Figures 4b–4d. Because of this uncertainty, we did not model HGSs for Neotethys (see blank area of Figure 5). A cautionary test using present-day topography and crustal thickness suggested the overall torque ( $\bar{T}_{\text{HGS}}$ ) should be relatively unaffected by this omission. However, it does have an effect on the reliability of the modeled local stresses, since the situation of zero  $\bar{\sigma}_{\text{HGS}}$  is unrealistic.

### 3.7.1. Consequences of Including Dynamic Topography

The radial component of asthenospheric flow causes dynamic support of the lithosphere, termed dynamic topography, which changes the pressure at the lithospheric compensation depth. Dynamic topography alters the GPE field. We, therefore, expand our isostatic GPE calculation to allow for dynamic pressure at the compensation depth, to arrive at HGSs which incorporate the influence of dynamic topography ( $\bar{\sigma}_{\text{HGS,DT}}$ ).

Models of present and past dynamic topography have been made using different methods, from forward models of mantle convection driven by plate motions and slabs, to models backward advecting mantle densities from tomography, to hybrids of the two (Flament et al., 2013). However, there is only limited agreement between the modeled dynamic topography and observed residual topography, both in terms of pattern and amplitude; the models tend to overestimate topography at large ( $\sim 10,000$  km) wavelengths (Cowie & Kuszniir, 2018; Davies et al., 2019; Hoggard et al., 2016; Steinberger et al., 2019). Müller et al. (2018) evaluated multiple reconstructions by comparing the predictions of continental flooding to geological data on paleo-coastlines. We implement two of their dynamic topography models that appear to correspond well in terms of land fraction and spatial overlap (Figure 6): M1, the hybrid backward and forward model from Spasojevic and Gurnis (2012) and M7, a modification of the forward model by Barnett-Moore et al. (2017). Neither of the models includes a time slice at exactly 75 Ma, so we use their time frames of 80 Ma and 69 Ma from M1 and M7, respectively. For details on the computation of the dynamic topography contribution in the GPE, see Appendix A.

Since we consider both present-day and historic dynamic topography, the difference between them (Figures 6c and 6f) will dictate the magnitude of the effect the dynamic topography has on the HGSs. The patterns of the differential fields are mostly comparable, however, the amplitudes of M1 ( $\sim 1,150$  m) are significantly larger than those of M7 ( $\sim 500$  m). As the dynamic topography consists of relatively large wavelength features, the GPE gradients locally are relatively unaffected by dynamic topography and the resulting HGSs all resemble those where dynamic topography is not considered in Figure 5. However, the overall torques on the plate do differ.

We recognize that the overestimation of long-wavelength dynamic topography in the adopted models influences the overall HGS torque, which is mostly sensitive to the same long wavelengths in GPE. To take account of this, we introduce a scaling factor (ranging from 0% to 100%) on the dynamic topography amplitudes.

Present-day small-scale topographic features (e.g., erosional peaks and valleys) are most likely to have been formed between 75 Ma and the present. Features on this scale tend to be symmetrical, and so should not contribute significantly to the overall HGS torque. We remove their influence by applying a low-pass filter

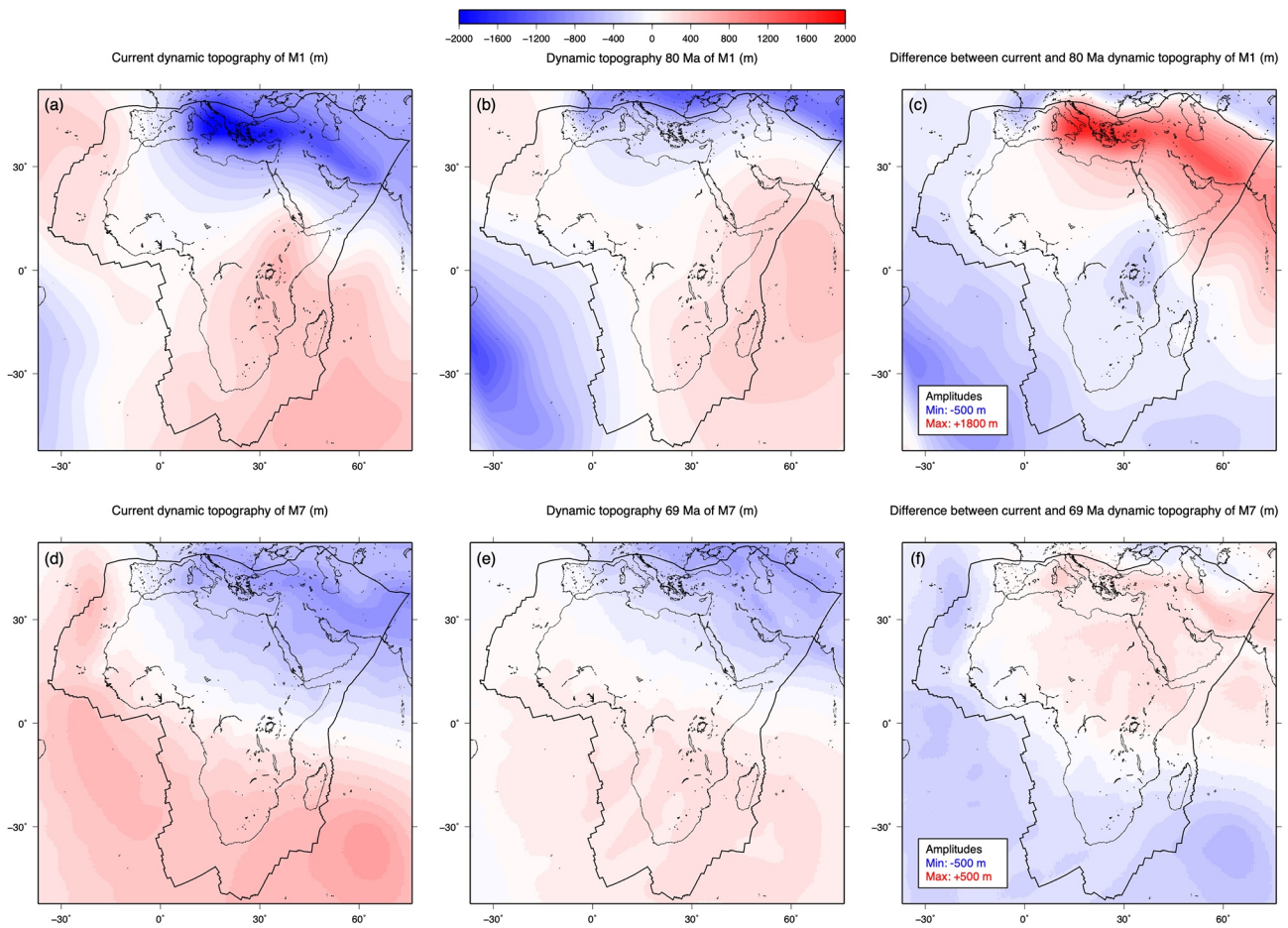


**Figure 6.** Dynamic topography models used in the calculation of the horizontal gravitational stresses, in the frame with Africa in its present-day position: model M1 (a and b) and model M7 (d and e), both from Müller et al. (2018). The differences between current and historic dynamic topography are plotted adjacently (c and f). The maximum and minimum amplitudes in the differential fields are also given.

to the HGSs. The low-pass filter applied excludes wavelengths smaller than 100 km. The influence of the choice of low-pass filter cutoff is explored in Section 5.3.

### 3.8. Exploring the Solution Space

Only three scaling factors in Equation 2 can be constrained, given the three-dimensionality of the torque balance equations. However, our model contains more than three unknown parameters (scaling factors and model choices). We, therefore, employ a grid sampling of the solution space, exploring the full range of parameter values that satisfies torque balance. The complete solution space is nine dimensional: the scaling factors of net slab pull, plate contact resistance at the trench, transform resistance, ridge transform resistance, continental collision resistance and basal drag ( $F_{L,nspl}$ ,  $F_{L,pcr}$ ,  $F_{L,tf}$ ,  $F_{L,rtf}$ ,  $F_{L,cc}$ ,  $\tau_{dr}$ ), the choice between the two dynamic topography models of Figure 6, the scaling of the dynamic topography amplitudes in those models, and the choice between the two absolute motion models. We employ the grid sampling in six dimensions and solve for the remaining  $F_{L,pcr}$ ,  $F_{L,tf}$ , and  $F_{L,cc}$  to achieve balanced torques. To ensure that we sample the solution space fully, we first perform tests of the approximate extent of the parameter ranges resulting in balance, and then choose the sampling ranges broadly around them. In defining the sampling ranges and solving for the scaling factors, we exclude unphysical negative scaling factors.

### 3.9. Intraplate Stress Modeling

To obtain the stress response of the force sets obeying torque balance, they are applied as discrete boundary conditions in solving the mechanical equilibrium equations with the GTECTON finite element code (version 2017.3.1; Govers & Meijer, 2001). Computation occurs on a fully elastic spherical shell using the formula of plane stress, with a Young's modulus of 100 GPa and a Poisson's ratio of 0.3, as averages for both the crustal and mantle part of the oceanic and continental lithosphere. The shell has a uniform thickness of 100 km, an estimate for the average lithospheric thickness, given the estimates that oceanic and continental lithosphere thicknesses are on average  $75 \pm 31$  km and  $134 \pm 64$  km (Steinberger & Becker, 2018). The plane stress formula results in the depth-averaged perturbations of the pre-stresses. GPE variations related to lateral lithospheric mantle thickness variations are likely small (Section 3.7). Vertically integrated horizontal stresses will thus remain constant when the thickness of the lithospheric mantle varies. Horizontal stresses are consequently lower in thicker lithosphere than in thinner lithosphere. This is not a problem in our study as we only have stress orientation observations to compare our modeled stresses with, not the magnitudes, so that accounting for lithospheric thickness variations to accurately model stress magnitudes is of limited importance.

We adopt an irregular triangular finite element grid containing 92,206 elements. We demonstrated that the adopted grid resolution is fine enough to smoothly resolve lateral stress gradients, and we conclude therefore that the models have converged. Our finite element method solves differential equations (the mechanical equilibrium equations), yielding changes in displacements and stresses in response to applied forces. Anchor points provide a necessary reference. To minimize stress concentrations near the anchors, we perform pilot experiments to carefully choose the locations for the anchors where the displacement gradients are low.

Elastic behavior captures the short-term response of rocks to tractions. It, thus, serves as the potential for permanent geological deformation by brittle and viscous mechanisms on longer timescales. We assume that away from major faults, on the spatial scales of the plate, the rheology will be roughly isotropic, so that principal stresses and strains align. In reality, relaxation of stress, be it either viscous in shear zones or by brittle slip on faults, can cause deviations of the stress orientations. When dealing with stress observations around major faults or shear zones, these deviations are important. However, we only have observations at the scales of the major rift zones and are interested in how well our imposed stresses can explain the presence of large-scale extension in them, so we are not concerned with the exact deviation of stresses locally. Potential oblique rifting is considered in the design of our misfit function (see Section 3.10 and Appendix B). Overall, we see the purely elastic rheology as a justifiable simplification of the lithospheric rheology for our purpose of evaluating the force models with the observations of rifting.

### 3.10. Fitting to Observations

We evaluate the parameter sets by comparing the modeled stress orientations to the geological observations (Figure 1), in order to find the parameter values resulting in the best-fitting models. The geological observations of rifting contain information on both the stress regime (normal) and the orientation of the principal horizontal stresses ( $S_{Hmin}$  perpendicular to the rifts). However, as discussed in Section 2, a component of oblique reactivation can be expected. We incorporate this observational uncertainty into the design of our misfit function ( $\phi$ ). We choose to be conservative in considering the strike-slip regime and an azimuthal discrepancy of  $45^\circ$  to represent the boundaries between good and bad fit. For details on the design of the misfit function, see Appendix B. To obtain the fit of single parameters values ( $p$ ), we compute the marginal probabilities ( $P(p)$ ), using a simplified version of the approach by Nijholt (2019):

$$P(p) = \frac{1}{N_p} \sum_{m=1}^{N_p} e^{-\frac{1}{2}\phi_m^2} \quad (3)$$

summing over the fits of all the balanced models ( $m$ ) that contain the particular parameter value ( $N_p$ ). In order to consider the fit of a combination of parameters ( $p_1, p_2$ ), we compute the 2D marginal probabilities:

$$P(p_1, p_2) = \frac{1}{N_{p_1, p_2}} \sum_{m=1}^{N_{p_1, p_2}} e^{-\frac{1}{2}\phi_m^2} \quad (4)$$

where  $N_{p_1, p_2}$  is the number of balanced models that contain both  $p_1$  and  $p_2$ .

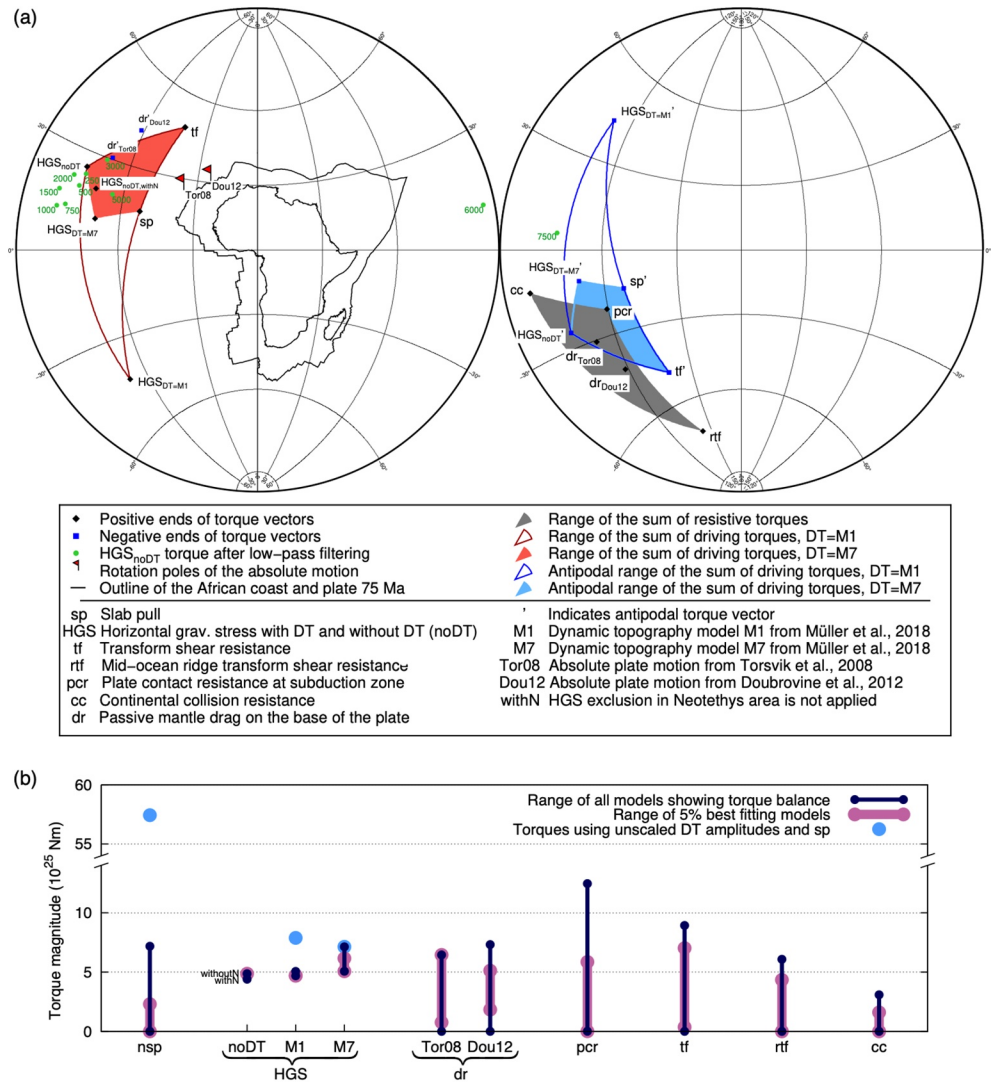


**Figure 7.** Torque directions (a) and magnitudes (b) acting on the African plate 75 Ma. (a) The torques are categorized either as driving (red) or resisting (gray) torques to aid the interpretation of torque balance, as described in the text. The torque directions of the horizontal gravitational stresses (HGS's) with and without the effect of dynamic topography are shown. As the dynamic topography amplitudes are scaled down, the influence of dynamic topography decreases and the  $\vec{T}_{\text{HGS,DT}}$  torques move in the direction of the  $\vec{T}_{\text{HGS,noDT}}$  torque. The effects of low-pass filtering the  $\vec{\sigma}_{\text{HGS,noDT}}$  tractions are illustrated for cutoff wavelengths of 250, 500, 600, 800, 1,100, and 1,600 km (green dots). The low-pass filtering cutoff for  $\vec{\sigma}_{\text{HGS,noDT}}$  as used in the main analysis is at 100 km. A HGS torque where the  $\vec{\sigma}_{\text{HGS,noDT}}$  exclusion in the Neotethys of Figure 5 is not applied, is also plotted ( $\vec{T}_{\text{HGS,noDT,withN}}$ ). (b) Full ranges of torque magnitudes that show balance and of magnitudes corresponding with the best-fitting models (as discussed in Section 4.3). To illustrate the influence of scaling the dynamic topography amplitudes and slab pull, HGS torque magnitudes with original dynamic topography amplitudes and the unscaled net slab pull torque magnitude (note the y-axis break) are shown too.

## 4. Results

### 4.1. Models Resulting in Torque Balance

The geometrical torques ( $\vec{T}$ ) in Equation 2 are computed from the line force and traction directions ( $\hat{f}$ ,  $\hat{\tau}$ ). Intersections between Earth's surface and positive ends of the torque vectors are displayed in Figure 7a. There appears to be two clusters of torques, which we categorize as either the driving or resisting torques, as the former aligns roughly with the direction of the absolute motion poles and the latter with the op-

posite direction. The HGS and (net) slab pull torques happen to be in roughly the same direction as the absolute plate motion, thus they are seen as driving the plate. Therefore, in the case of Africa 75 Ma, the HGs and slab pull forces were both driving the plate roughly north. The HGS torques that include the influence of dynamic topography ( $\vec{T}_{\text{HGS,DT=M1}}$  and  $\vec{T}_{\text{HGS,DT=M7}}$ ) deviate from the torque without dynamic topography influence ( $\vec{T}_{\text{HGS,noDT}}$ ), especially for the M1 model of Müller et al. (2018). As the torque of the transform shear traction is close to the absolute rotation pole (forces acting in roughly the same directions as the absolute motion), we choose to categorize the torque as driving. The driving nature of the transform forces in this case can also be recognized in Figure 2, with the relative motion along the Owen transform fault being in the direction of Africa's absolute motion. In other words, the shear tractions from the fast moving Indian plate were dragging Africa northward 75 Ma. On the other hand, the ridge transform torque is categorized as resisting, with the line forces on the ridge transform sections mostly resisting Africa's movement.

Figure 7a shows that the driving  $\vec{T}'_{\text{L,sp}}$ ,  $\vec{T}'_{\text{L,if}}$  and  $\vec{T}'_{\text{HGS}}$  torques are resisted by plate contact resistance at the trench ( $\vec{T}'_{\text{L,pcr}}$ ), passive mantle drag ( $\vec{T}'_{\text{dr}}$ ), ridge transforms ( $\vec{T}'_{\text{L,rtf}}$ ) and continental collision ( $\vec{T}'_{\text{L,cc}}$ ). The directions of the  $\vec{T}'_{\text{dr}}$  torques are not exactly opposite to their corresponding rotation poles, despite the passive drag being the reaction to the absolute motion. In Appendix C, we demonstrate that the passive drag torque does not necessarily have to be in exact opposition to the rotation axis if the rotation axis does not point approximately to the center of the plate. For Africa 75 Ma, the absolute rotation pole was located near the edge of the plate (Figure 2).

The overlap between the gray area spanned by resisting torques and the blue area spanned by antipodal driving torques in Figure 7a shows that, given the torque directions, there is potential for torque balance (Warners-Ruckstuhl et al., 2010). Since the torque magnitudes also turn out to be able to match, balanced torques are reached, with the overlap containing the complete solution space of the torque balance. The results of a grid sampling of the solution space are displayed in Figures 7b and 8, where Figure 8 shows the ranges of scaling parameters and Figure 7b the corresponding torque magnitude ranges (dark blue). Of the 345,092 parameter sets tested, 9,330 (2.7%) show torque balance.

For passive mantle drag and the line forces, a broad range of magnitudes is possible, yet the distribution of models showing balance is not uniform throughout the range, as is clear from the variable symbol size in Figure 8. In addition, both absolute motion models and dynamic topography models lead to balanced sets. When using the M1 dynamic topography model (Figures 6a–6c), balance only is possible if the dynamic topography amplitudes are scaled down significantly, to 30% or less, which corresponds to maximum amplitudes of approximately 350 m or less. Because the HGS torque magnitudes for the M1 model are within the same order of magnitude regardless of dynamic topography amplitude scaling (Figure 7b), the need for the strong amplitude scaling appears to be originating more from the deviating  $\vec{T}_{\text{HGS,DT=M1}}$  torque direction (Figure 7a) than from the torque magnitudes. For the M7 model (Figures 6d–6f), balance is possible regardless of the amplitude scaling. Overall, most balanced model sets include low amplitude dynamic topography. This apparent need for scaling down the dynamic topography amplitudes is in line with the common understanding that long wavelength dynamic topography is generally overestimated. Figure 6 shows that the African plate appears indeed to be located on a large wavelength dynamic topography structure

The most noteworthy result is that the average net slab pull magnitude needs to be  $\lesssim 2.2$  TN/m, corresponding to  $\leq 12.5\%$  of the average maximum slab pull magnitude of 17 TN/m. This indicates the presence of factors that strongly oppose or reduce slab pull. The scaling down of the net slab pull torque reduces its magnitude to the same order of magnitude as the other torques (Figure 7b).

#### 4.2. Fit to Observations

The solution space of possible force sets leads to a range of possible stress fields (see Figure 9a). For the majority of locations, fit between the modeled stresses and observations is possible. The Palmyride and Euphrates basins, Mozambique basin, and the western South African margin show a poor fit. The fit is especially poor for the Palmyride and Euphrates basins, which lie close to the region of removed HGS (Figure 5).

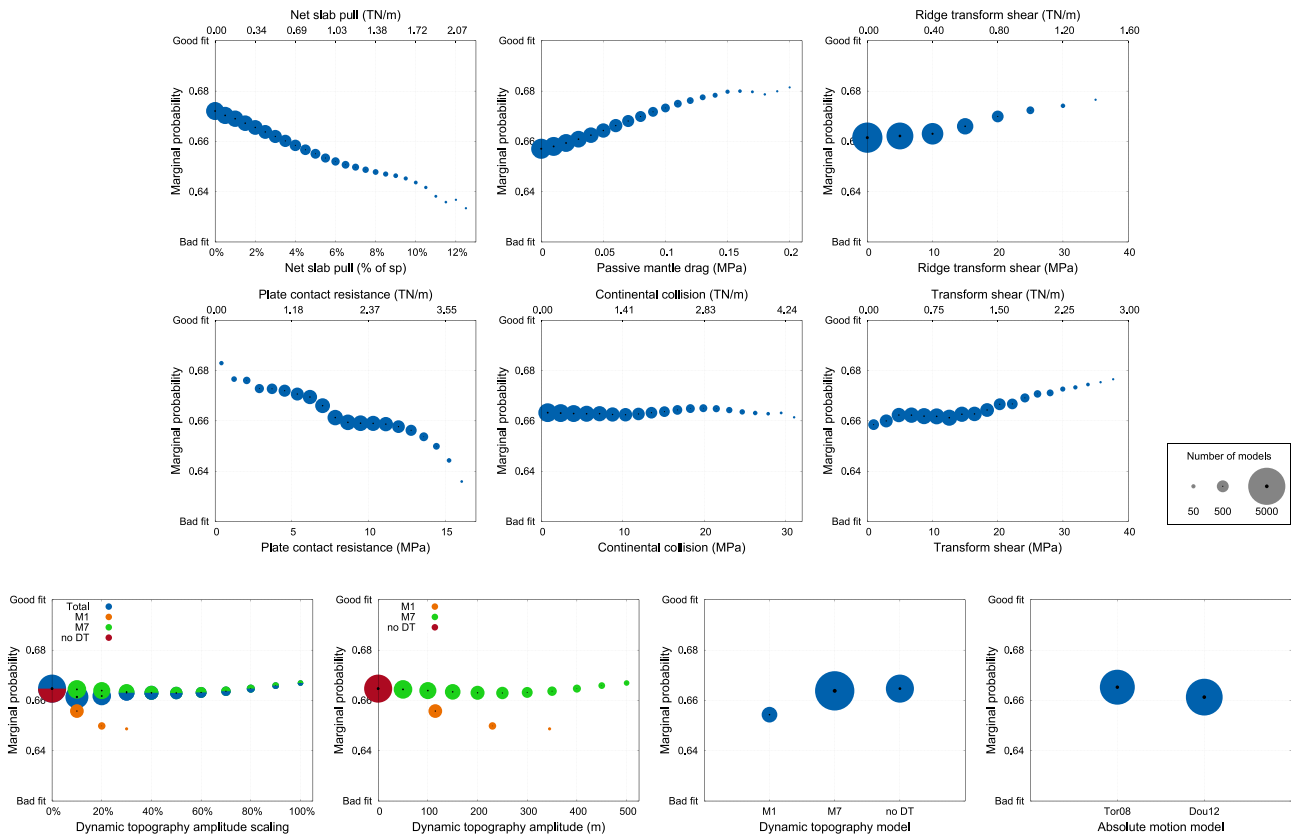


**Figure 8.** Marginal probabilities, as described in Section 3.10, for the parameters investigated in the grid sampling. Symbol size indicates the distribution of models throughout the ranges, that is, the number of models obeying torque balance for a given value. The edge force magnitudes (units of TN/m) are converted to approximate tractions (units of MPa) using the cross-sectional length ( $L$ ) of the assumed simplified plate contact geometries of Table 1. For the dynamic topography scaling, the probability distributions of both dynamic topography models are also plotted. To see how the scaling relates to the absolute amplitudes, the approximate dynamic topography amplitudes are plotted alongside. M1 and M7 are dynamic topography models by Müller et al. (2018) and Tor08 and Dou12 are moving hotspot frames by Torsvik et al. (2008) and Doubrovine et al. (2012).

Comparisons between modeled stress orientations and the observations are used to identify best-fitting models inside this range (details on the fit in Appendix B), and, thus, to identify the most likely parameter values (Figure 8). This analysis reinforces the torque balance result of low net slab pull, as the modeled stresses fit best when the net slab pull approaches zero. Estimates of other parameters are also advanced by the comparison to observations: strong passive mantle drag tractions, transform shear resistance and ridge transform resistance produce the best fits. Low values for plate contact resistance fit best. There is a slightly better fit when using the absolute motion of Torsvik et al. (2008) than that of Doubrovine et al. (2012). Using the M7 model by Müller et al. (2018) in the calculation of the dynamic topography component of the HGSs, results in better fits than using the M1 model. While the fit degrades with increasing dynamic topography amplitude for M1, the probability distribution for the M7 amplitude scaling is roughly flat. This is also the case for continental collision resistance and indicates that the modeled stresses are relatively insensitive to these two parameters, that is, their values cannot be constrained beyond the torque balance result.

The two-dimensional marginal probabilities (fits to observations) are shown in Figure 10a. They give an impression of the complex shape of the multidimensional torque balance solution space. They can also show possible parameter dependencies. Contour lines aid the identification of the dependencies, which if present should cause diagonal contours. However, pairs of independent parameters that both have a strong slope in the one-dimensional marginals (Figure 8) could lead to similarly diagonal contours, as the best fits would be located in one of the corners of the plot. Thus, we only consider the pairs of parameters as certainly interdependent if the diagonal pattern of interdependency is clearly resolvable within the torque balance solution (i.e., if the diagonal extreme is not situated along an edge of the solution space). In Figure 10a,

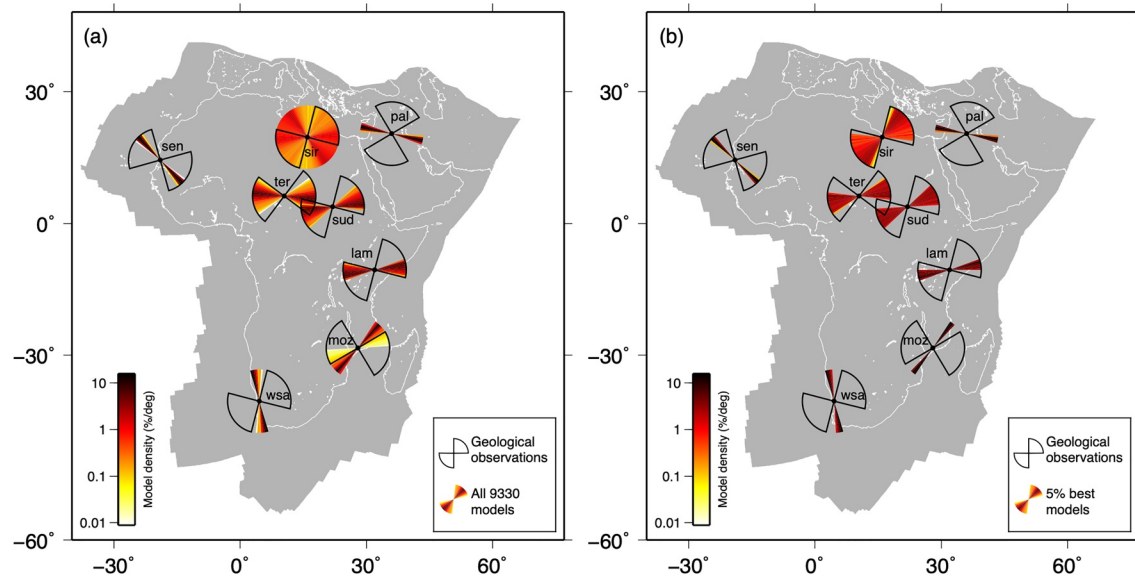


**Figure 9.** Comparison between modeled and observed  $S_{Hmin}$  directions for the modeled stress fields corresponding to all force sets with torque balance (a) and for only the 5% overall best-fitting models (b). The  $S_{Hmin}$  directions from geological observations are plotted as wedges to account for the observational uncertainty in stress orientation. For each location, the range of modeled  $S_{Hmin}$  directions is also plotted as wedges, with the wedges colored according to the model density. The model density represents the percentage of the total number of models per degree, so that most models line up in the dark colored directions. lam, Lamu embayment and Anza rift (Kenya); moz, Mozambique basins; pal, Palmyride and Euphrates basins (Syria); sen, Senegal basin; sir, Sirt basins (Libya); sud, Sudan rifts (South Sudan); ter, Termit trough (eastern Niger); wsa, western South African margin.

such patterns are clearest between mantle drag and continental collision, between mantle drag and plate contact resistance and between transform resistance and ridge transform resistance, where the former two pairs are anticorrelated and the latter is correlated. Both anticorrelations are between parameters related to resistive torques, while the correlated pair relate to one driving (transform) and one resistive (ridge transform) torque.

#### 4.3. Best-Fitting Models

The marginal probabilities of Figures 8 and 10a display the sensitivities of the modeled stresses to the parameters and show which parameter's values generally produce the best fits. However, simply selecting the parameter values with the higher marginal probabilities does not necessarily lead to the identification of one overall best-fitting model. In our case, a model chosen this way does not even show torque balance.

To get a better image of the characteristics of the high-scoring models, we explore the subset of the best-fitting 5% of the balanced models (466 models). The stress orientations of this subset show obvious improvements at locations that already showed a good fit (Figure 9). The fits in the remaining locations remain poor. The two dimensional probabilities of the best 5% are displayed in Figure 10b. They show the smaller ranges of parameters associated with the best models. These ranges (Table 2) indeed do not all align with results of the marginal probabilities: where Figure 8 indicates that the magnitudes of mantle drag, transform and ridge transform resistance should be relatively large for good fits, the best 5% of models comprise a wide range of values, indicating an insensitivity of the fit to these parameters. Other parameters do show higher sensitivity, as only a portion of the full torque balance range is included in the range of the subset of best-fitting models. These are net slab pull, plate contact resistance, continental collision and dynamic topography scaling of both the M1 and M7 models, with values of  $\leq 0.7$  TN/m ( $\leq 4\%$  of sp),  $\leq 7.6$  MPa,  $\leq 16$  MPa and  $\leq 10\%$  ( $\leq 115$  m) for M1, and  $\leq 60\%$  ( $\leq 300$  m) for M7. For all of these parameters (or pairs of them, as indicated by Figure 10b), best fits are produced when the values are small (or even zero), indicating that net slab pull, plate contact resistance tractions, continental collision tractions, and dynamic topography could have contributed little to torque balance and stress generation in the plate. However, the parameter values



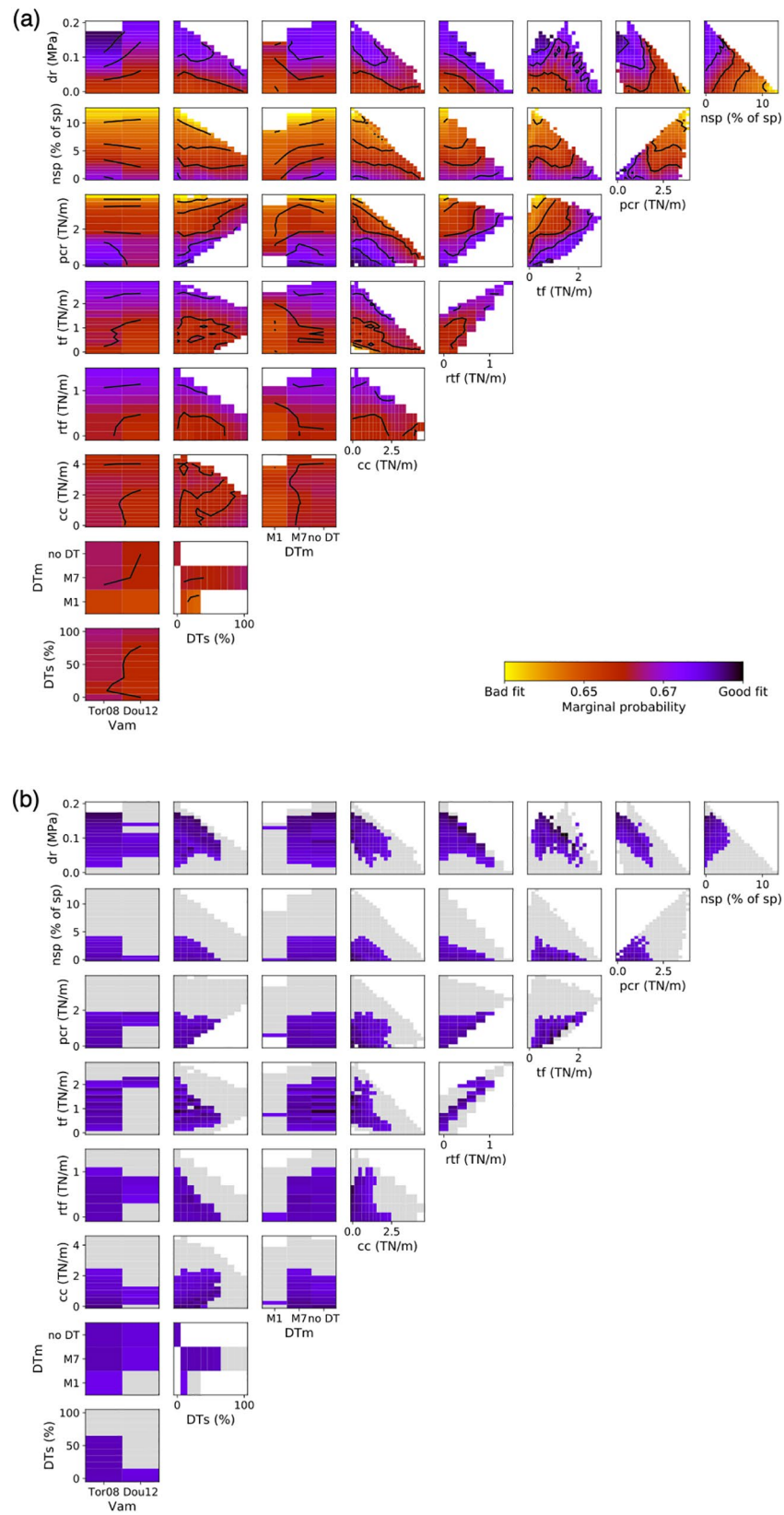


Figure 10

**Table 1**  
*Simplified Contact Geometries Corresponding to the Different Boundary Types*

Plate contact type	Contact geometry		
	$D$ (km)	$\alpha$ ( $^{\circ}$ )	$L$ (km)
Continental collision	100	45	141
Plate contact at subduction zone	100	25	236
Transform	75	90	75
Ridge transform	40	90	40

*Note.* The surface areas of the contacts are approximated using estimates for the depth extent of the contact ( $D$ ), the dip angle of the contact ( $\alpha$ ), and the resulting cross-sectional length ( $L$ ) perpendicular to the boundary. The  $D$  values are taken from the averages of lithospheric thicknesses for different tectonic regimes from Steinberger and Becker (2018): orogenic continent for the plate contacts at continental collision and subduction zones, intermediate age ocean for transform boundaries and young ocean for ridge transform boundaries.

could not have all been zero at the same time, as this would not result in torque balance.

The marginal probabilities of Figure 10b also show clearer parameter trade-offs. We identify correlations of transform resistance with ridge transform resistance and, possibly, with plate contact resistance and anticorrelations of mantle drag with the dynamic topography amplitude scaling, continental collision resistance, transform resistance, plate contact resistance and, possibly, with ridge transform resistance.

In order to show both a representation of the stress fields associated with models that fit the observations well and the variability between those stress fields, stresses from two of the 5% best-fitting models are plotted in Figure 11. We choose to display the model that scores absolute best and the model that scores worst of the 5% best-fitting models, that is, the models ranked 1st and 466th. The parameter values for these two models are given in Table 2. The variability of some of the parameter values illustrates how the fit between the observations and stresses is insensitive to these parameters. An example is the difference in transform resistance traction magnitude between the two models of Figure 11 (20.4 vs. 3.3 MPa), associated with large stress magnitude differences along the

Owen transform fault. In general, the stress orientations and stress regime patterns, with normal regimes mostly in continental parts, are comparable between the two models, while the stress magnitudes differ substantially between them. This is not surprising, as our fit to observations is only based on stress orientation and regime, not magnitude.

## 5. Discussion

### 5.1. Cause of the Low Net Slab Pull

Given the torques of Figure 7, the large magnitude slab pull torque needs to be scaled down to an average net slab pull magnitude of  $\lesssim 2.2$  TN/m, amounting to  $\leq 12.5\%$  of the maximum slab pull (Figure 8), in order to achieve torque balance on the plate. For the 5% best-fitting models, our net slab pull is even smaller, at  $\leq 4\%$  of the maximum slab pull. Forsyth and Uyeda (1975) find similar low net slab pull values for the current plates and attribute their results to large resistive shear tractions on the slabs (as in Figure 3b). They suspect the resistive tractions are velocity dependent, and their large magnitudes, thus, arise from fast sinking rates of the slabs (6–9 cm/yr). This concept of prevalent low net slab pull is not universally supported by focused studies of subduction models, plate dynamics and global plate motions (Table 3). Anyway, if we assume that the velocity-dependence of the tractions originates from linear viscosity that is similar along all slabs, the resistive traction on the slower ( $\sim 3$  cm/yr) sinking Neotethys slab must have been 50%–67% smaller (and even smaller in a nonlinear case). We, therefore, think that there needs to be another reason for the low net slab pull here. In light of the complex geometry of microcontinents interacting with the subduction as reconstructed by Stampfli and Borel (2004) and Van Hinsbergen et al. (2019), we propose that mechanisms like those in Figures 3c–3e are responsible for the additional slab pull loss. Identifying which of the mechanisms were occurring at the time is beyond the aims of this study. What is clear, though, is that it is unlikely that there was a continuous, purely oceanic, north-dipping Neotethys slab attached to Africa as reconstructed in Seton et al. (2012).

Alternatively, with torque directions that differ from those of Figure 7a, balanced torques could be achieved without scaling down the slab pull magnitude. For example, if either the direction of the slab pull torque or the antipodal basal drag torque (or both) were significantly different, they could overlap and a strong

**Figure 10.** 2D marginal probabilities for the parameters investigated in the grid search. Probabilities are plotted for all models (a), with contour lines to aid the identification of parameter dependencies, and for the best 5% of the models (b). Plots of (b) use the same color bar as (a) and the distribution of all models is plotted behind in gray. Abbreviations of the parameters are the same as in Figure 7a, with the addition of the absolute motion model (Vam), the dynamic topography model (DTm), and dynamic topography amplitude scaling (DTs).

**Table 2**  
Parameter Values of the Two Models Selected From the 5% Best Models, Which are Both Displayed in Figure 11, and the Full Ranges of the Parameter Values of the 5% Best Models (Figure 10b)

Model rank	nsp (%)	nsp (TN/m)	dr (MPa)	pcr (MPa)	tf (MPa)	rft (MPa)	cc (MPa)	DTm	DTs (%)	DTs (m)	Vam
1	0	0	0.11	4.0	20.4	15	0.1	-	0	0	Tor08
466	1.5	0.3	0.08	3.3	3.3	0	12.7	M7	20	100	Tor08
Range											
Min	0	0	0.02	0.02	1.5	0	0.02	M1	0	0	Tor08
Max	4	0.7	0.17	7.6	30	25	16	M7	60	300	Dou12

basal drag traction could balance the strong slab pull. In order for the slab pull torque to move toward the antipodal basal drag torque, it would need to move to the northwest. The direction of the slab pull torque depends on the geometry of slabs attached to Africa, as deduced from plate kinematic reconstructions, in our case from Seton et al. (2012). We do not see indications in other reconstructions by Stampfli et al. (2002) and Van Hinsbergen et al. (2019) for significant slab length in the western part of the Neotethys boundary, which is required to move the torque west. On the contrary, mature subduction zones with slabs attached to Africa are confined to the eastern part of the Neotethys boundary (Arabia-Europe boundary) in these reconstructions. So, deviation of the slab pull torque in the direction of the basal drag torque is unlikely. For the basal drag, we test two different absolute motion models, resulting in similar basal drag torques (Figure 7). If we take the difference between the two basal drag torque directions as a rough estimate of the directional uncertainty, an antipodal basal drag torque in the direction of the slab pull torque could just be possible. But even though this possibility exists, it requires a deviation in a very specific direction. Therefore, we prefer the lowering of the net slab pull (Figure 3), related to the tectonic setting, as the mechanism enabling torque balance in the presence of the large magnitude slab pull torque.

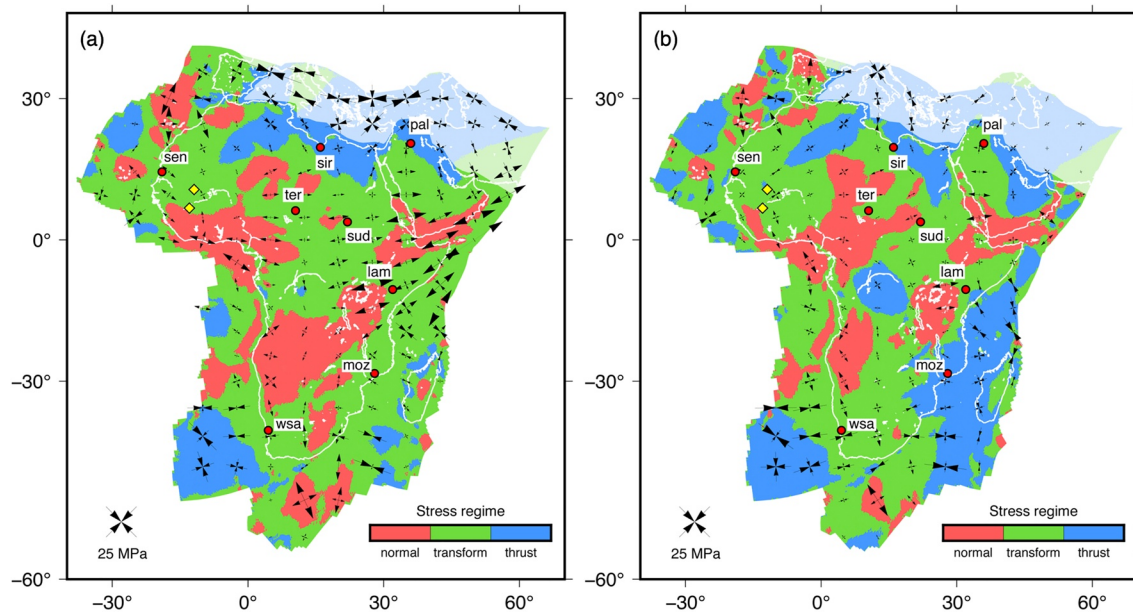


**Figure 11.** Modeled depth-averaged stress perturbations for the African plate 75 Ma for the model that is ranked 1st (a) and the model ranked 466th (b) out of all 9,330 balanced models. Arrows represent the principal horizontal stresses and colors show the distribution of the stress regimes. Red dots denote the locations of rifting observations and yellow diamonds the locations of the anchor points used in the modeling. lam, Lamu embayment and Anza rift (Kenya); moz, Mozambique basins; pal, Palmyride and Euphrates basins (Syria); sen, Senegal basin; sir, Sirt basins (Libya); sud, Sudan rifts (South Sudan); ter, Termit trough (eastern Niger); wsa, western South African margin.

**Table 3**  
*Compilation of Studies That Have Modeled Net Slab Pull Compared With This Study*

Study	Description	$\frac{F_{L,nspl}}{F_{L,sp}}$
Becker et al. (1999)	Analog and numerical subduction model	>60%
Schellart (2004)	Analog subduction model	8%–12%
Conrad and Lithgow-Bertelloni (2002)	Fitting absolute motions globally	>70%
Capitanio et al. (2009)	Numerical subduction model	38%–82%
Wortel et al. (1991)	Pacific plate dynamics	~7%
Govers and Meijer (2001)	Juan de Fuca plate dynamics	37%–90%
Forsyth and Uyeda (1975)	Global plate dynamics	12% <sup>a</sup>
This study	African plate dynamics	≤12.5%
	Fit with stresses	≤4%

<sup>a</sup>The later statistical analysis by Backus et al. (1981) showed that the uncertainty in the results of Forsyth and Uyeda (1975) was large, with a value of 0% lying within the range of uncertainty.

## 5.2. Torques Driving Absolute Motion

At any point of time, the forces on a plate govern its absolute motion. Given the lack of a significant angular momentum in a tectonic plate, the system does not have a “memory” of the movement that happened prior to any point in time. Therefore, there should be a torque that ensures that the absolute plate motion remains practically constant at any point of time, acting on the plate as if it were to accelerate the plate from standstill (or, similarly, from a minor slowdown) into its constant absolute motion. This torque, which we call  $\vec{T}^*$ , is composed of the torques from all forces that influence the absolute motion. This obviously includes the classical driving torques of slab pull and HGS (including ridge push). For Africa 75 Ma, the transform shear likely also contributed to  $\vec{T}^*$ , given the alignment between its torque and the absolute rotation axis (Figure 7a). However, torques from resisting forces can also influence the direction of a plate’s motion. For example, resistive shear tractions between neighboring plates, like the ridge transform tractions in our case, can introduce an additional rotational component to the plate motion in all cases except where those forces are aligned exactly in opposition to the absolute velocity. In our current model setup we cannot definitively distinguish the (components of the) tectonic forces that (contribute to) drive the plate motion from those that exist simply as a reaction to the motion, our current torque balance approach is not capable of quantitatively resolving the  $\vec{T}^*$  torque. A model of the plate’s kinematic and dynamic response to imposed driving forces, with velocity-dependent shear tractions, like that of Stotz et al. (2017), is required, but this is beyond the scope of this study.

## 5.3. HGS Uncertainties

Our analysis of the dynamics of the African plate 75 Ma shows that the HGSs were important in both the torque balance (Figure 7) and in the formation of the stress pattern (Figure 11). Uncertainties in the calculation of the HGSs arise from the lack of data of the past topography and crustal thickness, with the largest uncertainties around the plate’s northern Neotethyan boundary. Figure 7a shows that the influence of this area on the overall HGS torque direction appears to be small, as is evident from the minor deviation of the  $\vec{T}'_{HGS,DT,withN}$  torque, which includes the HGSs in the northern area, from the one where this area is excluded ( $\vec{T}'_{HGS,DT}$ ) as in Figure 5. Even though the overall torque seems to be relatively insensitive to the uncertainty in the Neotethys area, using appropriate paleotopography and paleo crustal thicknesses would be preferred to properly resolve the stresses regionally. This could reduce the misfit of stresses close to the Neotethyan margin, at the Palmyride and Euphrates basins (Figure 9). For a large part of the rest of the plate, the

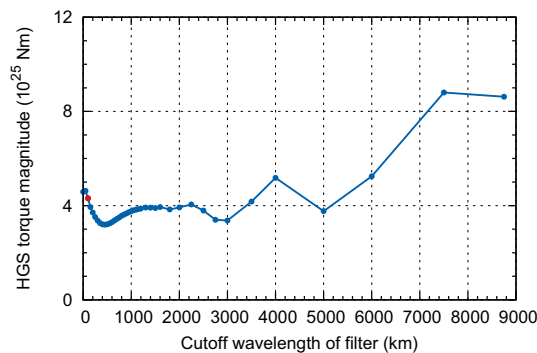


**Figure 12.** Influence of filtering short wavelength horizontal gravitational stresses (HGSs) (all wavelengths smaller than the cutoff wavelength) on the corresponding overall HGS torque magnitude. The red dot indicates the preferred filtering, used to calculate HGSs in the main analysis.

Figure 7a indicate that the torque is relatively unaffected by wavelengths of 5,000 km and smaller. When also filtering wavelengths of 6,000 km or larger from the HGS field, the torques deviate significantly, both in magnitude and orientation. The cause of this deviation lies in the large cutoff wavelengths approaching the width of the plate, which is roughly 5,500 km at its narrowest. So, filtering out all signals up to these large wavelengths essentially causes all information in the HGS field related to the real topography and crustal thickness to be lost.

Even though the HGS torque magnitude and direction appear to be insensitive to short wavelength topography, small-scale topography could have still been important for the eventual stress field pattern. However, the stress fields display only minor differences between a case without filtering and one where wavelengths smaller than 250 km are removed. This shows that uncertainties in small-scale features do not propagate to the stresses. The results indicate that for future studies aiming to reconstruct paleo-topography for Africa with the intent to calculate horizontal stresses induced by GPE variations, resolving small-scale topographic features will be unnecessary, especially those smaller than 250 km.

#### 5.4. Importance of Basal Shear From the Convective Mantle

Basal tractions are modeled as passive drag, assuming a hypothetical stationary mantle. Here, we evaluate that assumption, by exploring the possible effect of the shear tractions from the convective mantle (active drag) on torque balance and on the fit between the modeled stresses and the strain observations. Stresses induced by shear from the mantle should be similar to the horizontal stresses associated with dynamic topography, although with magnitudes that are about twice as large (Steinberger et al., 2001). In our grid search analysis, we scale the dynamic topography amplitudes, so, even though we do not model active drag specifically, the impact of active drag could be partly incorporated in our model through the dynamic topography. Following this approximation for active drag, a strong coupling between the convective mantle and the lithosphere would lead to high scaling factors for the dynamic topography amplitudes (potentially > 100%). The torque balance results and fit distributions of Figures 8 and 10 do not indicate that high scaling factors are preferred. Thus, a strong coupling between convective mantle and lithosphere is unlikely and we do not see a need for adjusting our model of the African plate 75 Ma to incorporate active drag.

## 6. Conclusions

The tectonic forcing on the African plate 75 Ma balances slab pull and HGSs with continental collision, plate contact resistance at the trench, ridge transform resistance and mantle drag forces (Figure 7a). The transform shear traction from the fast-moving Indian plate likely was one of the drivers of African plate motion.

The intra-plate stress orientations and regimes best match the strain observations when the average net slab pull is low, at  $\lesssim 0.7$  TN/m, that is,  $\leq 4\%$  of the maximum possible slab pull (17 TN/m). In addition, small magnitudes of plate contact resistance on the megathrust ( $\leq 7.6$  MPa) and continent collision tractions ( $\leq 16$  MPa) result in the best fits (Table 2). The fit to observations is relatively insensitive to the traction magnitudes of mantle drag, transform resistance and ridge transform resistance.

The net slab pull magnitude of  $\leq 4\%$  is low in comparison to other studies, especially given the low sinking rate of the slab. This indicates that there likely was no continuous, purely oceanic, north-dipping Neotethys slab 75 Ma. Instead, the Neotethyan convergent zone was likely more complex owing to the involvement of microcontinents in the plate convergence zone, which may have led to slab detachment, subduction polarity reversal or even continental subduction, likely leading to shorter slabs (Figure 3). The best fits to observations are achieved when the amplitudes of dynamic topography in the two models we investigated are relatively low, at 300 m or less.

Topography and crustal thickness variations on spatial scales smaller than the plate width contribute to local stress variations, but not to the overall plate dynamics.

### Appendix A: Details on the Horizontal Gravitational Stress Computation

For the isostatic part of the calculation, the density and pressure distribution in the lithosphere is constructed by balancing the crustal thickness and topography variations with a variable density of the lithospheric mantle. Loading by the water column above both continental and oceanic lithosphere is also included. The isostatic compensation depth is taken to be at the base of the reference continental lithosphere. Thickness of the oceanic lithosphere is approximated from the oceanic ages (Figure 4a) using the GDH1 cooling model (Stein & Stein, 1992), with asthenosphere underlying the oceanic lithosphere. The transitions from thinned continental to oceanic lithosphere are based on the plate reconstructions of Figure 4a. Densities of the water, crust and asthenosphere layers are assumed to be constant at 1,000, 2,850, and 3,200 kg/m<sup>3</sup>.

The calculation steps for the gravitational potential energy (GPE) including the effect of dynamic topography are displayed in Figure A1. We first remove present-day dynamic topography and calculate the GPE of that column isostatically, and then add the GPE contribution of the dynamic topography 75 Ma (rotated to the present-day frame). The resulting GPE field is rotated to Africa's position of 75 Ma and horizontal gravitational stresses are computed.

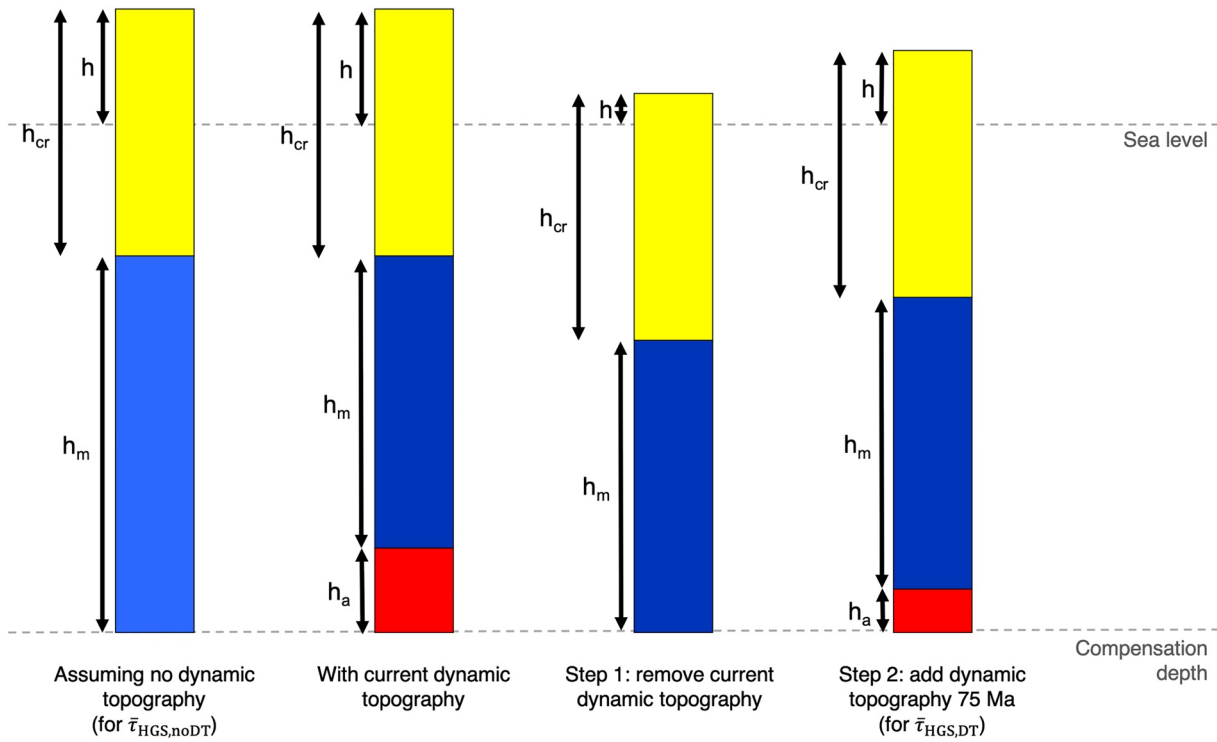


**Figure A1.** Schematic illustrations of the isostatic columns for the steps of the gravitational potential energy (GPE) calculation with consideration of dynamic topography (Figure 6). Here  $h$ ,  $h_{cr}$ ,  $h_m$ , and  $h_a$  stand for topography, crustal thickness, thickness of the lithospheric mantle, and the thickness of asthenosphere above the compensation depth (dynamic topography). The first column shows an apparent isostatic situation of thickened continent given data on the  $h$  and  $h_{cr}$  (Figures 4b and 4d) and the assumption of no dynamic topography, as it is used in the calculation of Nijholt et al. (2018). In reality, the  $h_m$  is different (here smaller) due to dynamic topography, introducing a column of asthenospheric mantle to our formula of isostasy, whose presence requires the density of  $h_m$  to differ too (as indicated by the brightness change). To compute the GPE field 75 Ma with dynamic topography, we apply a two-step approach. In the first step, the present-day dynamic topography is removed and the corresponding GPE of this column is calculated in the purely isostatic way from Nijholt et al. (2018). Then, the dynamic topography 75 Ma and its corresponding asthenospheric contribution ( $h_a$ ) is added. In this example, the dynamic topography is positive both for the present-day and 75 Ma situation, but the calculation is the same for other combinations of dynamic topography signals. Similarly, although thickened continent is shown here, the calculation steps are the same for thinned continent and oceanic parts, with their corresponding isostatic calculations following Nijholt et al. (2018).

## Appendix B: Functions for Fitting Stresses to Observations

In order to quantify the comparison between modeled stresses and geological observations, we adopt a misfit function ( $\phi$ ). Since the observations contain information on both the stress regimes and stress orientations (azimuths) at the observation locations (see Figure 1), we compute the misfits for both ( $\phi_{reg}$  and  $\phi_{azi}$ ).

We determine the stress regime using the regime index ( $R'$ ) as defined by Delvaux et al. (1997):

$$\begin{aligned} R' &= R && \text{when } \bar{\sigma}_1 \text{ is vertical (normal stress regime)} \\ R' &= 2 - R && \text{when } \bar{\sigma}_2 \text{ is vertical (transform stress regime)} \\ R' &= 2 + R && \text{when } \bar{\sigma}_3 \text{ is vertical (reverse stress regime)} \end{aligned} \quad (\text{B1})$$

where  $\bar{\sigma}_1$ ,  $\bar{\sigma}_2$  and  $\bar{\sigma}_3$  are the principal stresses ordered from most compressive to most tensile and  $R$  is the stress ratio (Bott, 1959), based on the principal stress magnitudes:

$$R = \frac{\sigma_2 - \sigma_3}{\sigma_1 - \sigma_3} \quad (\text{B2})$$

For the relation between  $R'$  values (ranging from 0 to 3) and the stress regimes, see Figure B1.

Because all observations are related to extensional features, we deem modeled tensile stresses at the observation locations to represent good fits. However, stresses that consist of both a tensile and strike-slip compo-

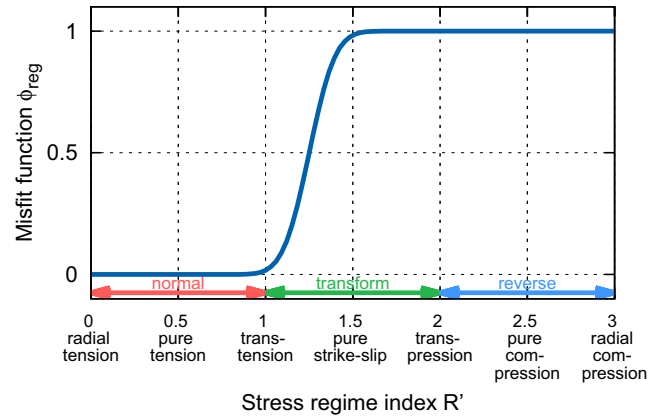


**Figure B1.** Misfit function for comparing the modeled stress regimes to observations. Stress regimes are calculated following Delvaux et al. (1997).

ment, could also be responsible for reactivation of rift faults. Reactivation should only be expected not to be occurring if the modeled stresses are pure strike-slip or reverse. In the design of the misfit function for the stress regime ( $\phi_{reg}$ ), we use an error function as the transition from the pure strike-slip and reverse regimes with a large misfit to the normal regimes with no misfit (Figure B1). For each location  $i$ , we calculate the misfit, which is of the form:

$$\phi_{reg, i} = \frac{\text{erf}\left(6\left(R' - 1.25\right)\right) + 1}{2} \quad (\text{B3})$$

The misfit function for the stress azimuth ( $\phi_{azi}$ ) is constructed in a similar way. The modeled most tensile horizontal stress ( $S_{Hmin}$ ) is compared to the extension directions of Figure 1, with  $\Delta azi$  being the difference between the two directions. As described in Section 2, oblique rifting could have been responsible for the observed extension, meaning that the actual extension directions could have deviated from the rift trend orthogonal directions of Figure 1. Sets of small intra-rift normal faults tend to form in oblique rifting settings (Withjack & Jamison, 1986). These faults could be overlooked as indicators for the oblique rifting, especially because they tend to rotate and align with the rift trend as extension progresses, when obliqueness is less than  $45^\circ$  (McClay & White, 1995). If obliqueness is large, sets of intra-rift strike-slip faults tend to form, instead the normal faults (Withjack & Jamison, 1986), causing the structures to be more obviously related to strike-slip settings. We take a conservative estimate of the possible obliqueness and regard a  $\Delta azi$  of  $45^\circ$  as the boundary between good fit and misfit (Figure B2). For each location the azimuthal misfit is calculated with:

$$\phi_{azi, i} = \frac{\text{erf}\left(15\left(\frac{\Delta azi - 35}{90}\right)\right) + 1}{2} \quad (\text{B4})$$

For each model, the misfits are averaged over the locations and the azimuthal and regime misfits are combined into the single misfit function  $\phi$ :

$$\phi = \frac{\sqrt{\left(\frac{\sum_{i=1}^{N_{obs}} \phi_{reg, i}}{N_{obs}}\right)^2 + \left(\frac{\sum_{i=1}^{N_{obs}} \phi_{azi, i}}{N_{obs}}\right)^2}}{2} \quad (\text{B5})$$

where  $N_{obs}$  is the number of observation locations, in our case  $N_{obs} = 8$ .



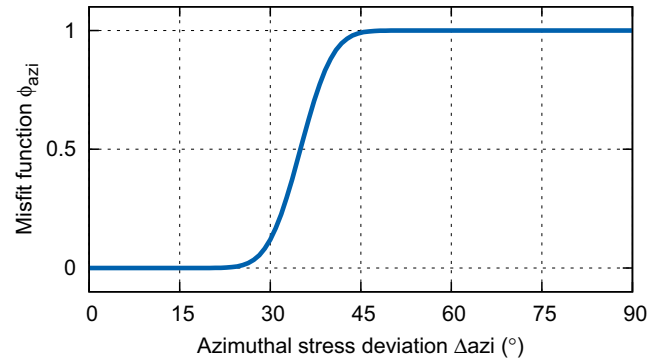


**Figure B2.** Misfit function for comparing the modeled  $S_{\text{Hmin}}$  directions to the extension directions of the observations of Figure 1.

### Appendix C: Relationship Between the Passive Drag Torque and Absolute Plate Motion

Passive drag tractions at the base of the lithosphere originate from the resistance to absolute plate motion by a hypothetical stationary mantle. Locally, this means that the passive drag tractions directly oppose the velocity. Here, we explore the effect of passive drag on an entire plate, via the relationship between the rotation axis of absolute motion and the passive drag torque in an idealized setting with homogeneous linear mantle viscosity.

The (local) absolute velocities of a plate rotating with respect to the selected mantle reference frame are defined by:

$$\vec{v} = \vec{\omega} \times \vec{r} \quad (\text{C1})$$

where  $\vec{\omega}$  is the angular velocity vector of the absolute motion, which pierces the Earth's surface at its corresponding rotation pole, and  $\vec{r}$  is the position vector from the center of the Earth to a given point on the plate. If the passive shear traction magnitude is assumed to be proportional to this velocity (linear mantle viscosity), the traction is given by:

$$\vec{\tau}_{\text{dr}} = -k\vec{v} \quad (\text{C2})$$

where  $k$  is a proportionality constant. The total torque of the passive basal drag is then computed from integration over the plate area ( $S$ ):

$$\begin{aligned} \vec{T}_{\text{dr}} &= \int_S \vec{r} \times \vec{\tau}_{\text{dr}} \, dS \\ &= -k \int_S \vec{r} \times (\vec{\omega} \times \vec{r}) \, dS \\ &= -k \int_S \left[ (\vec{r} \cdot \vec{r})\vec{\omega} - (\vec{r} \cdot \vec{\omega})\vec{r} \right] dS \\ &= -k |\vec{r}|^2 S \vec{\omega} + k \int_S (\vec{r} \cdot \vec{\omega}) \vec{r} \, dS \end{aligned} \quad (\text{C3})$$

So, the passive drag torque ( $\vec{T}_{\text{dr}}$ ) will only align with  $\vec{\omega}$  if the integration of the second part of this last equation happens to produce a vector in the direction of  $\vec{\omega}$ . This integration over the scaled  $\vec{r}$  vectors results in a vector pointing approximately to the center of the plate. So, only if  $\vec{\omega}$  also points to the center, will  $\vec{T}_{\text{dr}}$  and  $\vec{\omega}$  become antipodal.

### Data Availability Statement

Input and output files that were used for the models of this paper are digitally stored in the Yoda repository of the Utrecht University (<https://doi.org/10.24416/UU01-Y3YGRR>), in compliance with the FAIR principles.

## Acknowledgments

Careful and insightful reviews by Peter Molnar and Bernhard Steinberger helped to improve the manuscript. All map figures were generated using Generic Mapping Tools (Wessel et al., 2019). Marius C. Wouters was partially funded by project NWO DEEP.NL.2018.052. The authors thank Lukas van der Wiel for his continuous support with the GTECTON numerical model code and Paul Meijer for his comments on an earlier version of this manuscript.

## References

- Abadi, A. M., van Wees, J. D., van Dijk, P. M., & Cloetingh, S. A. (2008). Tectonics and subsidence evolution of the Sirt Basin, Libya. *AAPG Bulletin*, 92(8), 993–1027. <https://doi.org/10.1306/03310806070>
- Artyushkov, E. V. (1973). Stresses in the lithosphere caused by crustal thickness inhomogeneities. *Journal of Geophysical Research*, 78(32), 7675–7708. <https://doi.org/10.1029/JB078i032p07675>
- Backus, G., Park, J., & Garbasz, D. (1981). On the relative importance of the driving forces of plate motion. *Geophysical Journal of the Royal Astronomical Society*, 67, 415–435. <https://doi.org/10.1111/j.1365-246X.1981.tb02758.x>
- Barnett-Moore, N., Hassan, R., Müller, R. D., Williams, S. E., & Flament, N. (2017). Dynamic topography and eustasy controlled the paleogeographic evolution of northern Africa since the mid-Cretaceous. *Tectonics*, 36, 929–944. <https://doi.org/10.1002/2016TC004280>
- Beck, R. A., Burbank, D. W., Sercombe, W. J., Khan, A. M., & Lawrence, R. D. (1996). Late cretaceous ophiolite obduction and paleocene india-asia collision in the westernmost himalaya. *Geodinamica Acta*, 9(2), 114–144. <https://doi.org/10.1080/09853111.1996.11105281>
- Becker, T. W., Faccenna, C., O'Connell, R. J., & Giardini, D. (1999). The development of slabs in the upper mantle: Insights from numerical and laboratory experiments. *Journal of Geophysical Research*, 104(B7), 15207–15226. <https://doi.org/10.1029/1999jb900140>
- Behn, M. D., Boettcher, M. S., & Hirth, G. (2007). Thermal structure of oceanic transform faults. *Geology*, 35(4), 307–310. <https://doi.org/10.1130/G23112A.1>
- Bosworth, W., Guiraud, R., & Kessler, L. G. (1999). Late Cretaceous (ca. 84 Ma) compressive deformation of the stable platform of northeast Africa (Egypt): Far-field stress effects of the “Santonian event” and origin of the Syrian arc deformation belt. *Geology*, 27(7), 633–636. [https://doi.org/10.1130/0091-7613\(1999\)027<0633:LCCMCD>2.3.CO;2](https://doi.org/10.1130/0091-7613(1999)027<0633:LCCMCD>2.3.CO;2)
- Bosworth, W., & Morley, C. K. (1994). Structural and stratigraphic evolution of the Anza rift, Kenya. *Tectonophysics*, 236, 93–115. [https://doi.org/10.1016/0040-1951\(94\)90171-6](https://doi.org/10.1016/0040-1951(94)90171-6)
- Bosworth, W., & Stockli, D. F. (2016). Early magmatism in the greater Red Sea rift: Timing and significance. *Canadian Journal of Earth Sciences*, 53, 1158–1176. <https://doi.org/10.1139/cjes-2016-0019>
- Bott, M. H. P. (1959). The mechanics of oblique slip faulting. *Geological Magazine*, 96(2), 109–117. <https://doi.org/10.1017/S0016756800059987>
- Brew, G., Best, J., Barazangi, M., & Sawaf, T. (2003). Tectonic evolution of the NE Palmyride mountain belt, Syria: The Bishri crustal block. *Journal of the Geological Society*, 160, 677–685. <https://doi.org/10.1144/0016-764902-161>
- Brune, S. (2014). Evolution of stress and fault patterns in oblique rift systems: 3-D numerical lithospheric-scale experiments from rift to breakup. *Geochemistry, Geophysics, Geosystems*, 15, 3392–3415. <https://doi.org/10.1002/2014GC005446>
- Buffett, B. A. (2006). Plate force due to bending at subduction zones. *Journal of Geophysical Research*, 111, B09405. <https://doi.org/10.1029/2006JB004295>
- Buffett, B. A., & Becker, T. W. (2012). Bending stress and dissipation in subducted lithosphere. *Journal of Geophysical Research*, 117, B05413. <https://doi.org/10.1029/2012JB009205>
- Capitanio, F. A., Morra, G., & Goes, S. (2009). Dynamics of plate bending at the trench and slab-plate coupling. *Geochemistry, Geophysics, Geosystems*, 10(4). <https://doi.org/10.1029/2008GC002348>
- Capitanio, F. A., Morra, G., Goes, S., Weinberg, R. F., & Moresi, L. (2010). India-Asia convergence driven by the subduction of the Greater Indian continent. *Nature Geoscience*, 3, 136–139. <https://doi.org/10.1038/ngeo725>
- Chapple, W. M., & Tullis, T. E. (1977). Evaluation of the forces that drive the plates. *Journal of Geophysical Research*, 82(14), 1967–1984. <https://doi.org/10.1029/JB082i014p01967>
- Coblentz, D. D., & Richardson, R. M. (1995). Statistical trends in the intraplate stress field. *Journal of Geophysical Research*, 100(B10), 20245–20255. <https://doi.org/10.1029/95JB02160>
- Coblentz, D. D., & Richardson, R. M. (1996). Analysis of the South American intraplate stress field. *Journal of Geophysical Research*, 101(B4), 8643–8657. <https://doi.org/10.1029/96jb00090>
- Coblentz, D. D., Sandiford, M., Richardson, R. M., Zhou, S., & Hillis, R. (1995). The origins of the intraplate stress field in continental Australia. *Earth and Planetary Science Letters*, 133, 299–309. [https://doi.org/10.1016/0012-821X\(95\)00084-P](https://doi.org/10.1016/0012-821X(95)00084-P)
- Coblentz, D. D., Zhou, S., Hillis, R. R., Richardson, R. M., & Sandiford, M. (1998). Topography, boundary forces, and the Indo-Australian intraplate stress field. *Journal of Geophysical Research*, 103(B1), 919–931. <https://doi.org/10.1029/97jb02381>
- Conrad, C. P., Bilek, S., & Lithgow-Bertelloni, C. (2004). Great earthquakes and slab pull: Interaction between seismic coupling and plate-slab coupling. *Earth and Planetary Science Letters*, 218, 109–122. [https://doi.org/10.1016/S0012-821X\(03\)00643-5](https://doi.org/10.1016/S0012-821X(03)00643-5)
- Conrad, C. P., & Hager, B. H. (1999). Effects of plate bending and fault strength at subduction zones on plate dynamics. *Journal of Geophysical Research*, 104(B8), 17551–17571. <https://doi.org/10.1029/1999jb900149>
- Conrad, C. P., & Lithgow-Bertelloni, C. (2002). How mantle slabs drive plate motions. *Science*, 298, 207–209. <https://doi.org/10.1126/science.1074161>
- Conrad, C. P., & Lithgow-Bertelloni, C. (2006). Influence of continental roots and asthenosphere on plate-mantle coupling. *Geophysical Research Letters*, 33, L05312. <https://doi.org/10.1029/2005GL025621>
- Copley, A., Avouac, J.-P., & Royer, J.-Y. (2010). India-Asia collision and the Cenozoic slowdown of the Indian plate: Implications for the forces driving plate motions. *Journal of Geophysical Research*, 115, B03410. <https://doi.org/10.1029/2009JB006634>
- Corfield, R. L., Searle, M. P., & Pedersen, R. B. (2001). Tectonic setting, origin, and obduction history of the Spontang Ophiolite, Ladakh Himalaya, NW India. *The Journal of Geology*, 109, 715–736. <https://doi.org/10.1086/323191>
- Cowie, L., & Kuszniir, N. (2018). Renormalisation of global mantle dynamic topography predictions using residual topography measurements for “normal” oceanic crust. *Earth and Planetary Science Letters*, 499, 145–156. <https://doi.org/10.1016/j.epsl.2018.07.018>
- Davies, D. R., Valentine, A. P., Kramer, S. C., Rawlinson, N., Hoggard, M. J., Eakin, C. M., & Wilson, C. R. (2019). Earth's multi-scale topographic response to global mantle flow. *Nature Geoscience*, 12, 845–850. <https://doi.org/10.1038/s41561-019-0441-4>
- Delvaux, D., Moeys, R., Stapel, G., Petite, C., Levi, K., Miroshnichenko, A., et al. (1997). Paleostress reconstructions and geodynamics of the Baikal region, Central Asia, Part 2. Cenozoic rifting. *Tectonophysics*, 282, 1–38. [https://doi.org/10.1016/S0040-1951\(97\)00210-2](https://doi.org/10.1016/S0040-1951(97)00210-2)
- Dobrovine, P. V., Steinberger, B., & Torsvik, T. H. (2012). Absolute plate motions in a reference frame defined by moving hot spots in the Pacific, Atlantic, and Indian oceans. *Journal of Geophysical Research*, 117, B09101. <https://doi.org/10.1029/2011JB009072>
- England, P., & Houseman, G. (1985). Role of lithospheric strength heterogeneities in the tectonics of Tibet and neighbouring regions. *Nature*, 315, 297–301. <https://doi.org/10.1038/315297a0>
- England, P., & McKenzie, D. (1982). A thin viscous sheet model for continental deformation. *Geophysical Journal of the Royal Astronomical Society*, 70, 295–321. <https://doi.org/10.1111/j.1365-246x.1982.tb04969.x>

- England, P., & Wortel, R. (1980). Some consequences of the subduction of young slabs. *Earth and Planetary Science Letters*, 47, 403–415. [https://doi.org/10.1016/0012-821X\(80\)90028-X](https://doi.org/10.1016/0012-821X(80)90028-X)
- Flament, N., Gurnis, M., & Müller, R. D. (2013). A review of observations and models of dynamic topography. *Lithosphere*, 5(2), 189–210. <https://doi.org/10.1130/L245.1>
- Fleitout, L., & Froidevaux, C. (1982). Tectonics and topography for a lithosphere containing density heterogeneities. *Tectonics*, 1(1), 21–56. <https://doi.org/10.1029/TC001i001p00021>
- Forsyth, D., & Uyeda, S. (1975). On the relative importance of the driving forces of plate motion. *Geophysical Journal of the Royal Astronomical Society*, 43, 163–200. <https://doi.org/10.1111/j.1365-246X.1975.tb04143.x>
- Frank, F. C. (1972). Plate tectonics, the analogy with glacier flow, and isostasy. In H. C. Heard (Ed.), *Geophysical monograph series: Flow and fracture of rocks* (Vol. 16, pp. 285–292). AGU. <https://doi.org/10.1029/GM016p0285>
- Fukao, Y., & Obayashi, M. (2013). Subducted slabs stagnant above, penetrating through, and trapped below the 660 km discontinuity. *Journal of Geophysical Research: Solid Earth*, 118, 5920–5938. <https://doi.org/10.1002/2013JB010466>
- Fukao, Y., Obayashi, M., Nakakuki, T., & the Deep Slab Project Group. (2009). Stagnant slab: A review. *Annual Review of Earth and Planetary Sciences*, 37, 19–46. <https://doi.org/10.1146/annurev.earth.36.031207.124224>
- Gaina, C., Torsvik, T. H., van Hinsbergen, D. J., Medvedev, S., Werner, S. C., & Labails, C. (2013). The African plate: A history of oceanic crust accretion and subduction since the Jurassic. *Tectonophysics*, 604, 4–25. <https://doi.org/10.1016/j.tecto.2013.05.037>
- Globig, J., Fernández, M., Torne, M., Vergés, J., Robert, A., & Faccenna, C. (2016). New insights into the crust and lithospheric mantle structure of Africa from elevation, geoid, and thermal analysis. *Journal of Geophysical Research: Solid Earth*, 121, 5389–5424. <https://doi.org/10.1002/2016JB012972>
- Goes, S., Capitanio, F. A., Morra, G., Seton, M., & Giardini, D. (2011). Signatures of downgoing plate-buoyancy driven subduction in Cenozoic plate motions. *Physics of the Earth and Planetary Interiors*, 184, 1–13. <https://doi.org/10.1016/j.pepi.2010.10.007>
- Govers, R., & Meijer, P. T. (2001). On the dynamics of the Juan de Fuca plate. *Earth and Planetary Science Letters*, 189, 115–131. [https://doi.org/10.1016/S0012-821X\(01\)00360-0](https://doi.org/10.1016/S0012-821X(01)00360-0)
- Guiraud, R., & Bosworth, W. (1997). Senonian basin inversion and rejuvenation of rifting in Africa and Arabia: Synthesis and implications to plate-scale tectonics. *Tectonophysics*, 282(1–4), 39–82. [https://doi.org/10.1016/S0040-1951\(97\)00212-6](https://doi.org/10.1016/S0040-1951(97)00212-6)
- Guiraud, R., Bosworth, W., Thierry, J., & Delplanque, A. (2005). Phanerozoic geological evolution of Northern and Central Africa: An overview. *Journal of African Earth Sciences*, 43, 83–143. <https://doi.org/10.1016/j.jafrearsci.2005.07.017>
- Heidbach, O., Rajabi, M., Reiter, K., & Ziegler, M., & the WSM team. (2016). *World stress map database release*. GFZ Data Services.
- Hoggard, M. J., White, N., & Al-Attar, D. (2016). Global dynamic topography observations reveal limited influence of large-scale mantle flow. *Nature Geoscience*, 9, 456–463. <https://doi.org/10.1038/ngeo2709>
- Humphreys, E. D., & Coblenz, D. D. (2007). North American dynamics and western U.S. tectonics. *Reviews of Geophysics*, 45, RG3001. <https://doi.org/10.1029/2005RG000181>
- Jacoby, W. R. (1970). Instability in the upper mantle and global plate movements. *Journal of Geophysical Research*, 75(29), 5671–5680. <https://doi.org/10.1029/JB075i029p05671>
- Jagoutz, O., Royden, L., Holt, A. F., & Becker, T. W. (2015). Anomalously fast convergence of India and Eurasia caused by double subduction. *Nature Geoscience*, 8, 475–478. <https://doi.org/10.1038/NNGEO2418>
- Janssen, M. E., Stephenson, R. A., & Cloetingh, S. (1995). Temporal and spatial correlations between changes in plate motions and the evolution of rifted basins in Africa. *Geological Society of America Bulletin*, 107(11), 1317–1332. [https://doi.org/10.1130/0016-7606\(1995\)107<1317:TASCBC>2.3.CO;2](https://doi.org/10.1130/0016-7606(1995)107<1317:TASCBC>2.3.CO;2)
- King, S. D., Frost, D. J., & Rubie, D. C. (2015). Why cold slabs stagnate in the transition zone. *Geology*, 43(3), 231–234. <https://doi.org/10.1130/G36320.1>
- Kohlstedt, D., Evans, B., & Mackwell, S. (1995). Strength of the lithosphere: Constraints imposed by laboratory experiments. *Journal of Geophysical Research*, 100(B9), 17587–17602. <https://doi.org/10.1029/95JB01460>
- Lallemand, S., Heuret, A., & Boutelier, D. (2005). On the relationships between slab dip, back-arc stress, upper plate absolute motion, and crustal nature in subduction zones. *Geochemistry, Geophysics, Geosystems*, 6(9). <https://doi.org/10.1029/2005GC000917>
- Laske, G., Masters, G., Ma, Z., & Pasyanos, M. E. (2013). *Update on CRUST1.0—A 1-degree global model of Earth's crust* (Vol. 15, p. 2658). EGU General Assembly.
- Lliboutry, L. (1969). Sea-floor spreading, continental drift and lithosphere sinking with an asthenosphere at melting point. *Journal of Geophysical Research*, 74(27), 6525–6540. <https://doi.org/10.1029/JB074i027p06525>
- Macchiavelli, C., Vergés, J., Schettino, A., Fernández, M., Turco, E., Casciello, E., et al. (2017). A new Southern North Atlantic isochron map: Insights into the drift of the Iberian Plate since the Late Cretaceous. *Journal of Geophysical Research: Solid Earth*, 122, 9603–9626. <https://doi.org/10.1002/2017JB014769>
- McClay, K. R., & White, M. J. (1995). Analogue modelling of orthogonal and oblique rifting. *Marine and Petroleum Geology*, 12, 137–151. [https://doi.org/10.1016/0264-8172\(95\)92835-K](https://doi.org/10.1016/0264-8172(95)92835-K)
- Meijer, P. T., & Wortel, M. J. R. (1992). The dynamics of motion of the South American Plate. *Journal of Geophysical Research*, 97(B8), 11915–11931. <https://doi.org/10.1029/91JB01123>
- Meijer, P. T., & Wortel, M. J. R. (1997). Present-day dynamics of the Aegean region: A model analysis of the horizontal pattern of stress and deformation. *Tectonics*, 16(6), 879–895. <https://doi.org/10.1029/97TC02004>
- Meijer, P. T., & Wortel, M. J. R. (1999). Cenozoic dynamics of the African plate with emphasis on the Africa-Eurasia collision. *Journal of Geophysical Research*, 104(B4), 7405–7418. <https://doi.org/10.1029/1999jb900009>
- Molnar, P., England, P. C., & Jones, C. H. (2015). Mantle dynamics, isostasy, and the support of high terrain. *Journal of Geophysical Research: Solid Earth*, 120, 1932–1957. <https://doi.org/10.1002/2014JB011724>
- Molnar, P., & Lyon-Caen, H. (1988). Some simple physical aspects of the support, structure, and evolution of mountain belts. In *Processes in continental lithospheric deformation* (Vol. 218, pp. 179–207). <https://doi.org/10.1130/spe218-p179>
- Moucha, R., & Forte, A. M. (2011). Changes in African topography driven by mantle convection. *Nature Geoscience*, 4, 707–712. <https://doi.org/10.1038/ngeo1235>
- Müller, R. D., Hassan, R., Gurnis, M., Flament, N., & Williams, S. E. (2018). Dynamic topography of passive continental margins and their hinterlands since the Cretaceous. *Gondwana Research*, 53, 225–251. <https://doi.org/10.1016/j.gr.2017.04.028>
- Neil, E. A., & Houseman, G. A. (1997). Geodynamics of the Tarim Basin and the Tian Shan in central Asia. *Tectonics*, 16(4), 571–584. <https://doi.org/10.1029/97TC01413>

- Niemeijer, A. R., Boulton, C., Toy, V. G., Townend, J., & Sutherland, R. (2016). Large-displacement, hydrothermal frictional properties of DFDP-1 fault rocks, Alpine Fault, New Zealand: Implications for deep rupture propagation. *Journal of Geophysical Research: Solid Earth*, *121*. <https://doi.org/10.1002/2015JB012593>
- Nijholt, N. (2019). *STEP faults and lithosphere dynamics in the Mediterranean* (Doctoral dissertation). Utrecht University. Retrieved from <https://dspace.library.uu.nl/handle/1874/386073>
- Nijholt, N., Govers, R., & Wortel, R. (2018). On the forces that drive and resist deformation of the south-central Mediterranean: A mechanical model study. *Geophysical Journal International*, *214*, 876–894. <https://doi.org/10.1093/gji/ggy144>
- Pallares, C., Maury, R. C., Bellon, H., Royer, J.-Y., Calmus, T., Aguillón-Robles, A., et al. (2007). Slab-tearing following ridge-trench collision: Evidence from Miocene volcanism in Baja California, México. *Journal of Volcanology and Geothermal Research*, *161*, 95–117. <https://doi.org/10.1016/j.jvolgeores.2006.11.002>
- Pérez-Díaz, L., & Eagles, G. (2014). Constraining South Atlantic growth with seafloor spreading data. *Tectonics*, *33*, 1848–1873. <https://doi.org/10.1002/2014TC003644>
- Pérez-Díaz, L., & Eagles, G. (2017). A new high-resolution seafloor age grid for the South Atlantic. *Geochemistry, Geophysics, Geosystems*, *18*, 457–470. <https://doi.org/10.1002/2016GC006750>
- Phillips, B. R., & Bunge, H. P. (2005). Heterogeneity and time dependence in 3D spherical mantle convection models with continental drift. *Earth and Planetary Science Letters*, *233*, 121–135. <https://doi.org/10.1016/j.epsl.2005.01.041>
- Richardson, R. M., & Reding, L. M. (1991). North American Plate dynamics. *Journal of Geophysical Research*, *96*(B7), 12201–12223. <https://doi.org/10.1029/91jb00958>
- Richter, F., & McKenzie, D. (1978). Simple plate models of mantle convection. *Journal of Geophysics*, *44*, 441–471.
- Sandiford, M., & Coblenz, D. (1994). Plate-scale potential-energy distributions and the fragmentation of ageing plates. *Earth and Planetary Science Letters*, *126*, 143–159. [https://doi.org/10.1016/0012-821X\(94\)90247-X](https://doi.org/10.1016/0012-821X(94)90247-X)
- Schellart, W. P. (2004). Quantifying the net slab pull force as a driving mechanism for plate tectonics. *Geophysical Research Letters*, *31*, L07611. <https://doi.org/10.1029/2004GL019528>
- Seton, M., Müller, R. D., Zahirovic, S., Gaina, C., Torsvik, T., Shephard, G., et al. (2012). Global continental and ocean basin reconstructions since 200 Ma. *Earth-Science Reviews*, *113*, 212–270. <https://doi.org/10.1016/j.earscirev.2012.03.002>
- Spasojevic, S., & Gurnis, M. (2012). Sea level and vertical motion of continents from dynamic earth models since the Late Cretaceous. *AAPG Bulletin*, *96*(11), 2037–2064. <https://doi.org/10.1306/03261211121>
- Stampfli, G. M., & Borel, G. D. (2004). The TRANSMED transects in space and time: Constraints on the paleotectonic evolution of the Mediterranean domain. In *The TRANSMED Atlas: The Mediterranean region from crust to mantle* (pp. 53–80). Springer. [https://doi.org/10.1007/978-3-642-18919-7\\_3](https://doi.org/10.1007/978-3-642-18919-7_3)
- Stampfli, G. M., Borel, G. D., Marchant, R., & Mosar, J. (2002). Western Alps geological constraints on western Tethyan reconstructions. *Journal of the Virtual Explorer*, *8*, 77–106. <https://doi.org/10.3809/jvirtex.2002.00057>
- Stamps, D. S., Iaffaldano, G., & Calais, E. (2015). Role of mantle flow in Nubia-Somalia plate divergence. *Geophysical Research Letters*, *42*, 290–296. <https://doi.org/10.1002/2014GL062515>
- Stefanick, M., & Jurdy, M. (1992). Stress observations and driving force models for the South American plate. *Journal of Geophysical Research*, *97*(B8), 11905–11913. <https://doi.org/10.1029/91JB01798>
- Stein, C. A., & Stein, S. (1992). A model for the global variation in oceanic depth and heat flow with lithospheric age. *Nature*, *359*, 123–129. <https://doi.org/10.1038/359123a0>
- Steinberger, B., & Becker, T. W. (2018). A comparison of lithospheric thickness models. *Tectonophysics*, *746*, 325–338. <https://doi.org/10.1016/j.tecto.2016.08.001>
- Steinberger, B., Conrad, C. P., Osei Tutu, A., & Hoggard, M. J. (2019). On the amplitude of dynamic topography at spherical harmonic degree two. *Tectonophysics*, *760*, 221–228. <https://doi.org/10.1016/j.tecto.2017.11.032>
- Steinberger, B., Schmelting, H., & Marquart, G. (2001). Large-scale lithospheric stress field and topography induced by global mantle circulation. *Earth and Planetary Science Letters*, *186*, 75–91. [https://doi.org/10.1016/S0012-821X\(01\)00229-1](https://doi.org/10.1016/S0012-821X(01)00229-1)
- Stotz, I. L., Iaffaldano, G., & Davies, D. R. (2017). Late Miocene Pacific plate kinematic change explained with coupled global models of mantle and lithosphere dynamics. *Geophysical Research Letters*, *44*, 7177–7186. <https://doi.org/10.1002/2017GL073920>
- Stotz, I. L., Iaffaldano, G., & Davies, D. R. (2018). Pressure-driven Poiseuille flow: A major component of the torque-balance governing Pacific plate motion. *Geophysical Research Letters*, *45*, 117–125. <https://doi.org/10.1002/2017GL075697>
- Torsvik, T. H., Müller, R. D., Voo, R. V. D., Steinberger, B., & Gaina, C. (2008). Global plate motion frames: Toward a unified model. *Reviews of Geophysics*, *46*, 1–44. <https://doi.org/10.1029/2007rg000227>
- Tron, V., & Brun, J. P. (1991). Experiments on oblique rifting in brittle-ductile systems. *Tectonophysics*, *188*, 71–84. [https://doi.org/10.1016/0040-1951\(91\)90315-J](https://doi.org/10.1016/0040-1951(91)90315-J)
- Tuck-Martin, A., Adam, J., & Eagles, G. (2018). New plate kinematic model and tectono-stratigraphic history of the East African and West Madagascan Margins. *Basin Research*, *30*, 1118–1140. <https://doi.org/10.1111/bre.12294>
- Van Benthem, S., & Govers, R. (2010). The Caribbean plate: Pulled, pushed, or dragged? *Journal of Geophysical Research*, *115*, B10409. <https://doi.org/10.1029/2009JB006950>
- Van Der Voo, R., Spakman, W., & Bijwaard, H. (1999). Tethyan subducted slabs under India. *Earth and Planetary Science Letters*, *171*, 7–20. [https://doi.org/10.1016/S0012-821X\(99\)00131-4](https://doi.org/10.1016/S0012-821X(99)00131-4)
- Van Hinsbergen, D. J., Hafkenscheid, E., Spakman, W., Meulenkamp, J. E., & Wortel, R. (2005). Nappe stacking resulting from subduction of oceanic and continental lithosphere below Greece. *Geology*, *33*(4), 325–328. <https://doi.org/10.1130/G20878.1>
- Van Hinsbergen, D. J., Torsvik, T. H., Schmid, S. M., Matenco, L. C., Maffione, M., Vissers, R. L., et al. (2019). Orogenic architecture of the Mediterranean region and kinematic reconstruction of its tectonic evolution since the Triassic. *Gondwana Research*, *81*, 79–229. <https://doi.org/10.1016/j.gr.2019.07.009>
- Van Summeren, J., Conrad, C. P., & Lithgow-Bertelloni, C. (2012). The importance of slab pull and a global asthenosphere to plate motions. *Geochemistry, Geophysics, Geosystems*, *13*(1). <https://doi.org/10.1029/2011GC003873>
- Viola, G., Kounov, A., Andreoli, M. A., & Mattila, J. (2012). Brittle tectonic evolution along the western margin of South Africa: More than 500 Myr of continued reactivation. *Tectonophysics*, *514–517*, 93–114. <https://doi.org/10.1016/j.tecto.2011.10.009>
- Vissers, R., & Meijer, P. (2012). Mesozoic rotation of Iberia: Subduction in the Pyrenees? *Earth-Science Reviews*, *110*, 93–110. <https://doi.org/10.1016/j.earscirev.2011.11.001>
- Warners-Ruckstuhl, K. N., Govers, R., & Wortel, R. (2012). Lithosphere-mantle coupling and the dynamics of the Eurasian Plate. *Geophysical Journal International*, *189*, 1253–1276. <https://doi.org/10.1111/j.1365-246X.2012.05427.x>

- Warners-Ruckstuhl, K. N., Govers, R., & Wortel, R. (2013). Tethyan collision forces and the stress field of the Eurasian Plate. *Geophysical Journal International*, 195, 1–15. <https://doi.org/10.1093/gji/ggt219>
- Warners-Ruckstuhl, K. N., Meijer, P. T., Govers, R., & Wortel, M. J. R. (2010). A lithosphere-dynamics constraint on mantle flow: Analysis of the Eurasian plate. *Geophysical Research Letters*, 37, L18308. <https://doi.org/10.1029/2010GL044431>
- Weatherall, P., Marks, K. M., Jakobsson, M., Schmitt, T., Tani, S., Arndt, J. E., et al. (2015). A new digital bathymetric model of the world's oceans. *Earth and Space Science*, 2, 331–345. <https://doi.org/10.1002/2015EA000107>
- Wessel, P., Luis, J. F., Uieda, L., Scharroo, R., Wobbe, F., Smith, W. H., & Tian, D. (2019). The generic mapping tools version 6. *Geochemistry, Geophysics, Geosystems*, 20, 5556–5564. <https://doi.org/10.1029/2019GC008515>
- Williams, S., Flament, N., Dietmar Müller, R., & Butterworth, N. (2015). Absolute plate motions since 130 Ma constrained by subduction zone kinematics. *Earth and Planetary Science Letters*, 418, 66–77. <https://doi.org/10.1016/j.epsl.2015.02.026>
- Withjack, M. O., & Jamison, W. R. (1986). Deformation produced by oblique rifting. *Tectonophysics*, 126, 99–124. [https://doi.org/10.1016/0040-1951\(86\)90222-2](https://doi.org/10.1016/0040-1951(86)90222-2)
- Wortel, M. J. R., & Cloetingh, S. (1981). On the origin of the Cocos-Nazca spreading center. *Geology*, 9, 425–430. [https://doi.org/10.1130/0091-7613\(1981\)9<425:OTOOTC>2.0.CO;2](https://doi.org/10.1130/0091-7613(1981)9<425:OTOOTC>2.0.CO;2)
- Wortel, M. J. R., Remkes, M. J. N., Govers, R., Cloetingh, S. A. P. L., & Meijer, P. T. (1991). Dynamics of the lithosphere and the intraplate stress field. *Philosophical Transactions of the Royal Society of London A*, 337, 111–126. <https://doi.org/10.1098/rsta.1991.0110>
- Wortel, M. J. R., & Spakman, W. (2000). Subduction and slab detachment in the Mediterranean-Carpathian region. *Science*, 290, 1910–1917. <https://doi.org/10.1126/science.290.5498.1910>
- Zoback, M. L. (1992). First- and second-order patterns of stress in the lithosphere: The world stress map project. *Journal of Geophysical Research*, 97(B8), 11703–11728. <https://doi.org/10.1029/92jb00132>